3rd Workshop Of
CODE_BRIGHT USERS

2nd June 2011
Barcelona, Spain

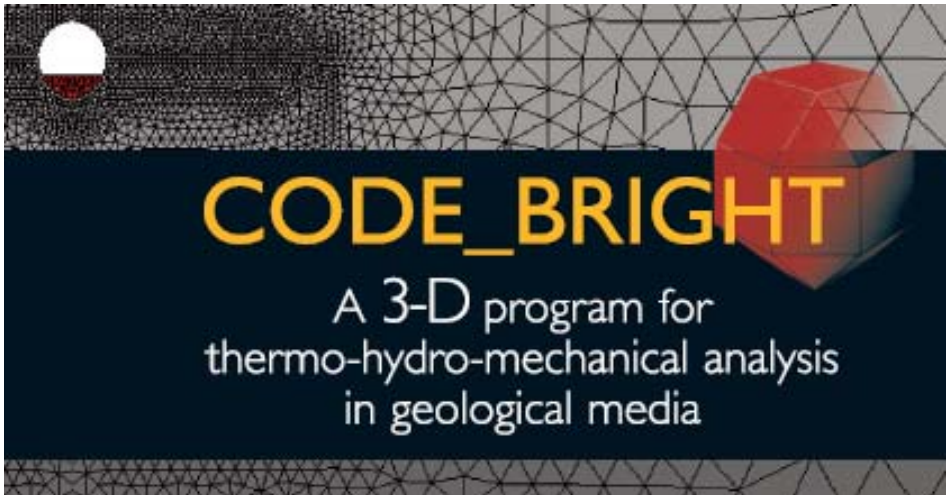

Department of Geotechnical Engineering and Geosciences
(UPC. Barcelona. Spain)
CIMNE
(Centro Internacional de Métodos Numéricos en Ingeniería.
Barcelona. Spain)

CODE_BRIGHT

A 3-D program for thermo-hydro-mechanical analysis in geological media

3RD WORKSHOP OF CODE_BRIGHT USERS

Barcelona, 2 June 2011

Department of Geotechnical Engineering and Geosciences

(UPC. Barcelona. Spain)

CIMNE

(Centro Internacional de Métodos Numéricos en Ingeniería. Barcelona. Spain)

CONTENTS

VALIDATION OF CONSTITUTIVE MODELS FOR DAMAGE AND SEALING OF CLAY ROCK

Chun-Liang ZHANG
Gesellschaft für Anlagen- und Reaktorsicherheit (GRS), D-38122 Braunschweig, Germany
e-mail: chun-liang.zhang@grs.de, web page: http://www.grs.de/

1 INTRODUCTION

With regard to the new German approach of the safe containment of radioactive waste in an isolating rock zone (IRZ), it is of paramount importance to confirm constitutive models enabling adequate prediction of the long-term processes prevailing in the host rock and the engineered barriers, particularly the evolution or self-sealing of the EDZ in interaction with the EBS. Since 2002, GRS uses the FEM code CODE-BRIGHT developed by UPC for the analysis of coupled thermo-hydro-mechanical processes in the multi-barrier-system around HLW repositories in clay and salt formations. In the framework of the EC TIMODAZ project performed from Oct. 2006 to Sept. 2010, GRS performed a series of benchmark modelling exercises and compared with laboratory observations. The main purpose of this was to validate the capabilities of the constitutive models available from CODE-BRIGHT for the prediction of the development and recovery of the EDZ in clay formations.

2 LABORATORY TESTS

GRS carried out laboratory tests on large hollow cylinders of the Callovo-Oxfordian clay rock (COX) to investigate fracturing and sealing processes of the host rock around disposal boreholes and to provide a data base for validation of constitutive models by benchmark exercise in the framework of TIMODAZ project. Large cores were extracted from the URL Bure and prepared to hollow cylinders of ~0.5 m length and 280 mm outer diameter with axially-drilled central boreholes of 100 mm diameter. Figure 1 illustrates the test layout and pictures of a large COX hollow cylinder before and after testing. In the tests, the relevant processes regarding damage development such as borehole excavation, backfilling, heating and cooling were simulated, whereby responses of the COX hollow cylinders were monitored by various instruments for measurements of external confining stress, axial / radial strain, borehole pressure / convergence, gas / water injection pressure, inflow / outflow, and temperature.

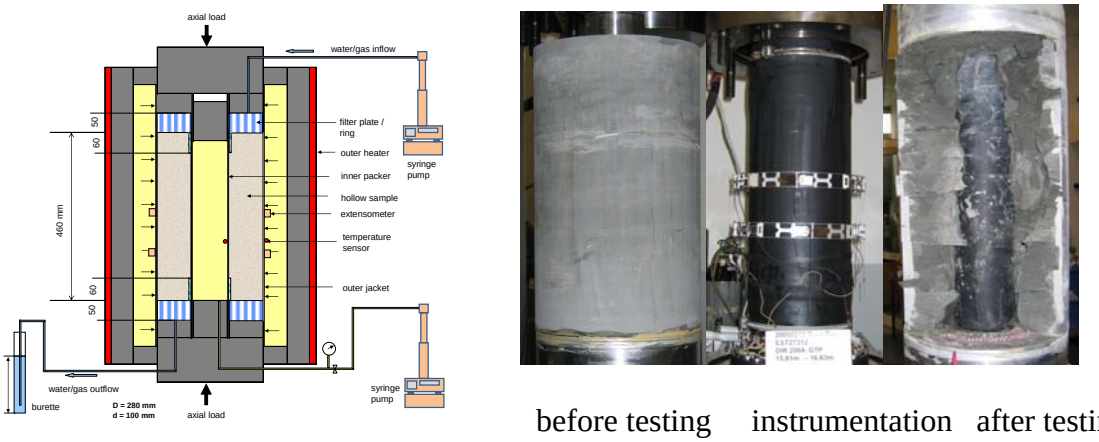

before testing instrumentation after testing

Fig. 1 Layout of a simulation test on a large hollow cylinder in GRS' big triaxial apparatus

The main observations are:

1. The borehole excavation simulated by reducing the inner pressure from 15 MPa down to 1 MPa resulted in a borehole convergence but not any increase in permeability along the cylinder axis, indicating no build up of pathway through the tested section of a half meter. A drastic increase of gas permeability (up to 10^{-14} m^2) was observed only by the external confining stress beyond 20 to 24 MPa (corresponding to rock depths between 800 and 1000 m). The interconnected macro-fractures were observed through the thick cylinder wall after testing.
2. The backfill impact simulated by increasing the borehole pressure from 1 to 15 MPa led to a strong reduction of the gas permeability by several orders of magnitude down to 10^{-17} to 10^{-21} m^2, depending on the initial characteristics of the fractures in the argillite.
3. The water transport through the fractures induced swelling of clay minerals into the interstices and caused a pronounced reduction of the intrinsic permeability. The permeability obtained by water flowing is about four orders of magnitude lower than that determined by gas flowing. The water permeability of $2.0 \cdot 10^{-18}$ m^{-2} was estimated.
4. Heating from 29 to 74°C accelerated the borehole convergence and the water inflow. The thermal impact on the water conductivity of fractured argillite is governed by the change of the water viscosity, while the intrinsic permeability is less affected by heating.
5. Cooling down slowed the deformation and the water transport through the fractured argillite. The permeability of $3.5 \cdot 10^{-18}$ m^2 estimated after cooling is almost the same as before heating.
6. The post-tests on the tested samples indicated a high adsorption potential of the argillite, under which a great amount of water can be taken up to 13% in unloaded conditions. This water content is much more than that in the natural and saturated argillite. The increase in water content reads to expansion of the argillite and sealing of the fractures under confined conditions.

3 NUMERICAL SIMULATION

1.1 Main Assumptions

Considering the complex testing procedure and boundary conditions of the large hollow cylinder tests, coupled THM calculations were carried out by solving a set of balance equations of energy, solid mass, water mass, air mass and stress equilibrium with selected constitutive models. The main assumptions were made:

1. The COX clay rock is relatively isotropic and homogeneous;
2. Heat transport includes conduction (Fourier's law) through the porous medium, advection of liquid water and vapour flow;
3. Water transport is controlled by liquid water advection (Darcy's law), vapour diffusion in air (Fick's law), and liquid / gas phase changes (psychrometric law);
4. Gas migration is governed by advection (Darcy's law), dissolution in liquid (Henry's law) and the ideal gas law;
5. The Kozeny's model is employed for the relationship of permeability with porosity;
6. The damage-elastoplastic model developed by UPC for argillaceous rocks is applied for description of the mechanical behaviour of the COX claystone. COX is considered as a composite material made of a clay matrix connected by bonds. The clay matrix behaves

like a typical elastoplastic soil Hoek and Brown's criterion as yield surface, while the bonds behave like a typical quasi-brittle material that can be represented by a damage elastic law. Bond damage or degradation occurs as the result of apparition of micro-fissures within the bonds, which reduces the surface on which stresses and strains are active. Any load applied to an element of cemented material is distributed itself between the soil matrix and the bonds according to a ratio that depends on the geometric arrangement of both components.

1.2 A modelling example

Test BMT1 was performed on a COX hollow cylinder of D/d/L= 280/100/525 mm at ambient temperature of 26 °C in four steps:

1. Initial state at the same outer and inner borehole pressure of $\sigma_R = \sigma_r = 15$ MPa and axial stress of $\sigma_a = 17$ MPa;
2. Borehole excavation by decreasing the inner pressure down to $\sigma_r = 2.6$ MPa;
3. Unloading in radial direction down to $\sigma_R = 3$ MPa for 4 days;
4. Loading in axial direction to failure.

During the test, gas flow was recorded at injection pressure of 1.5 MPa at the bottom. This test was simulated in a hydro-mechanical coupling way using an axisymmetric model. Because the sample was initially not saturated at a degree of 82 %, the corresponding suction of s = 22 MPa is adapted as the initial condition in the sample. The modelling steps with application of the corresponding boundary conditions are illustrated in Fig. 2.

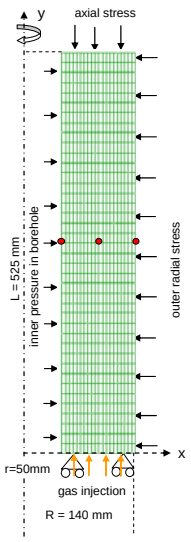

Calculation procedure:

Step 1: t = 0 – 0.9 day, pre-consolidation
temperature T = 26 °C
pore water pressure p_l = -22 MPa
gas injection pressure p_g = 1.5 MPa
vertical stress σ_y = 17 MPa
outer radial stress σ_R = 15 MPa
inner radial stress σ_r = 15 MPa

Step 2: t = 0.9 – 1.8 day, borehole excavation
inner radial stress from σ_r = 15 to 2 MPa

Step 3: t = 1.8 – 5.9 day, radial unloading
outer radial stress from σ_R = 15 to 3 MPa

Step 4: t = 5.9 – 6.0 day, axial loading
axial stress from σ_y = 17 MPa up to failure

Fig. 2 Geometry and boundary conditions for modelling of the hollow cylinder test BMT1

1.3 Results

The modelling results indicate that:

- The short-term deformation behaviour of the hollow cylinders is reasonably represented by the model with indication of micro-damage evolution, but the post-failure behaviour could not be modelled due to earlier stop of the computation (Fig. 3).

- The drastic increase in permeability by fracturing and the permeability decrease by re-compaction of the fractures can not be captured by the Kozeny's permeability – porosity relationship for porous media without fractures (Fig. 4).
- The observed water inflow into the fractured claystone is significantly underestimated by the modelling even though the real permeability value of the fractured claystone is used (Fig. 5).
- The significant responses of deformation in the damaged claystone to heating and cooling are weakly revealed by the modelling (Fig. 6)

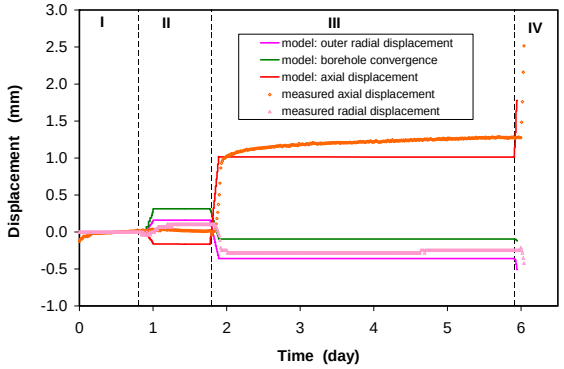

Fig. 3 Comparison of deformations between modelling results and test data

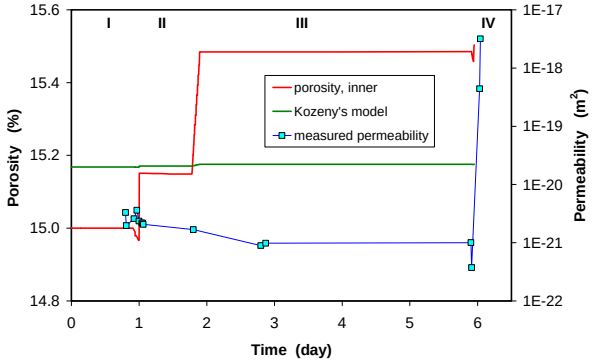

Fig. 4 Calculated permeability variations in comparison with the measured data

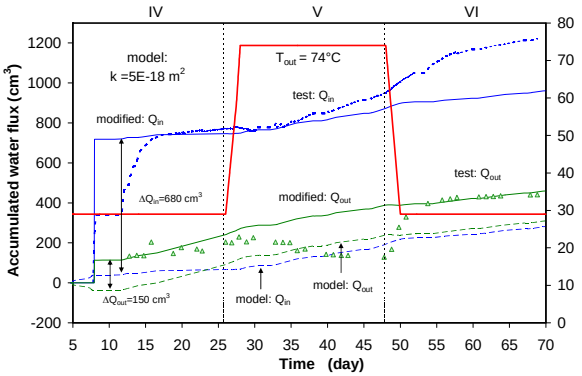

Fig. 5 Calculated and observed water flow before, during and after heating

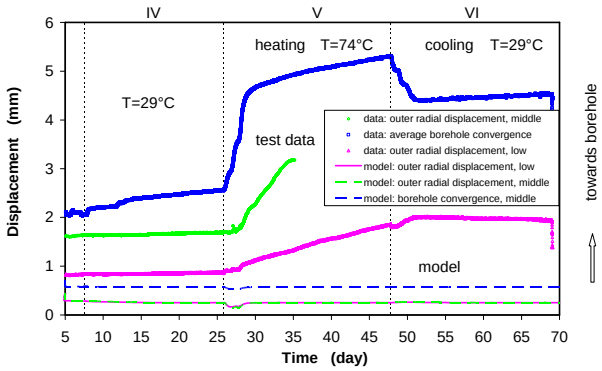

Fig. 6 Calculated and observed deformations before, during and after heating

4 CONCLUSION

The modeling results suggest that further improvement of the model predictability is necessary in regard to the following aspects:

- Mechanical damage evolution and criteria for permeability changes
- Self-sealing process of EDZ with permeability decrease due to both effects of mechanical re-compaction and moisture-induced swelling / slaking of clay matrix
- Time dependence of the rock deformation and compaction
- Relation of swelling with suction or water saturation and confining stress
- Thermal effects on the sealing of EDZ
- Anisotropic effects on the THM behaviour of EDZ.

The improvement of the applied models and/or development of new models for prediction of the damage and sealing process of EDZ in clay rocks will be conducted by GRS in the future.

HEAT FLOWS IN GAPS. RADIATION AND CONDUCTION

Pintado X. and Autio J.

B+TECH Oy, Laulukuja 4, FI-00420, Helsinki, Finland
e-mail: xavier.pintado@btech.fi

Key words: Nuclear waste repository, radiation, conduction, gap

Abstract. *The nuclear waste repository reference in Finland is constructed with bentonite blocks which are surrounded by gaps. The first gap is between the canister and the bentonite. The second gap is between the bentonite and the rock. These gaps are filled with different materials (air, water or clay). The thermal analysis has been done in order to compare the different situations options.*

1 INTRODUCTION

Compacted bentonite is used as a material to make barriers to prevent contamination isolating the contamination source. High-density compacted bentonite in the form of blocks, discs and rings has also been proposed as sealing material in high-level radioactive waste repositories, as it provides very low permeability, sufficient thermal conductivity and adequate mechanical resistance.

It is necessary to know what the maximum temperature in bentonite is because of there are some mineralogical changes from certain temperature which make the bentonite loss part of some properties. These changes must be avoided. The nuclear waste repository design spreads the nuclear waste canisters at the layout and the distance between canisters is one of the crucial parameter designs.

The maximum temperature depend the properties of the different components and the geometry. The gaps could have influence at the maximum bentonite temperature due the sudden change of medium properties although their small volume. The problem has been simulated with CODE_BRIGHT [1].

2 MODEL DESCRIPTION

2.1 Geometry

The geometry simulated has been a box with 12.5 m (half distance between tunnels), 5.5 m (half distance between deposition holes) and 37.75 m height. The deposition hole has 7.8 m deep and 1.75 m diameter and the canister 4.8 m length and 1.05 m diameter. There are two gaps in the buffer, the canister-bentonite gap with 10 mm thickness and the bentonite-rock with 35 mm thickness. The finite element mesh has 33812 nodes and 182957 elements.

2.2 Material parameters

It has been a thermal analysis, so the only parameters are the natural density, the specific heat and the thermal conductivity. There isn’t any liquid or gas flow, so the materials are considered as solids and the porosity is reduced to 0.01. These properties are the mean of the

mixture solid-liquid gas in the initial state. The canister thermal conductivity is extremely high in order to maintain constant temperature in it.

	Porosity	Natural density (kg/m^3)	Specific heat (J/kgK)	Thermal conductivity (W/mK)
Rock	0.01	2749	784	2.61
Canister	0.01	7874	450	8020
Backfill	0.01	1720	1208	0.544
Bentonite	0.01	1830	1287	0.906
Air	0.01	1.2	1012	0.03
Water	0.01	1000	4181	0.61

Table 1. Material properties

The radiation heat flow has to be taken into account in air. The radiant heat flux q_r from a non reflecting, perfectly absorbing surface of absolute temperature T is given by the Stefan-Boltzman's law:

$$\boldsymbol{q_r = \sigma \times T^4 = e \times \sigma \times T^4}$$

Where σ is the Stefan-Boltzman's constant: σ=5.6697x10^{-8} W/m^{2}K^4. This equation applies for an ideal blackbody radiation. For physical surfaces, the heat output is also controlled by the surface emissivity e [2].

The net radiant heat exchange between two gray surfaces where the gap is small compared the axial length and the radius is:

$$\boldsymbol{q_r = \frac{e_1 \times e_2}{e_1 + e_2 - e_1 \times e_2} \times \sigma \times 4 \times \left(T_1^4 - T_2^4\right)}$$

If the temperature difference between both surfaces is low, the heat flux is approximately:

$$\boldsymbol{q_r = \frac{e_1 \times e_2}{e_1 + e_2 - e_1 \times e_2} \times \sigma \times 4 \times T_2^3 \times \Delta T}$$

The thermal conductivity law is:

$$\boldsymbol{q_r = -\lambda \times \nabla T}$$

$\boldsymbol{|\nabla T|}$ is $\boldsymbol{\Delta T / \Delta l}$, so the coefficient for simulate the radiation heat transport as conductivity heat transport has to be multiplied by Δl. For a gap of 10 mm width, the emissivity of 0.52 [3] and a temperature of 80ºC, the effective thermal conductivity λ_{dry} is 0.101 W/mK, where the λ_{gas}=0.03 W/mK, related with the heat conductivity transport of heat, has already been added. It has to be into account this effective thermal conductivity increases linearly with the width of the gap.

2.3 Boundary conditions

The canister boundary condition is a constant heat flux (Von Neuman boundary condition) in five nodes which drops with time [3]. The total amount of heat is in figure 2.

The heat fluxes at vertical planes are zero for symmetry. The upper and lower planes have Dirichlet boundary conditions. The temperature changes by influence of the entire repository (see figure 3). These temperatures have been calculated with the analytical solution for a continuous media with segmental heat sources [3].

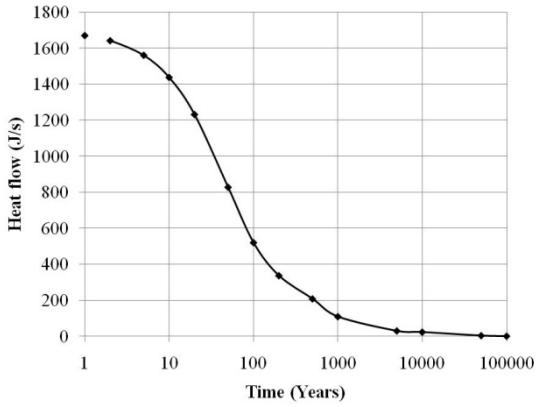

Figure 2. Heat flow

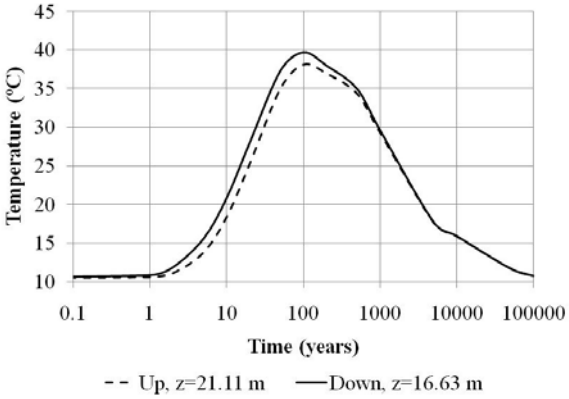

Figure 3. Temperature boundary conditions

3 SIMULATION RESULTS

The gap filling is one of the design issues. In order to study its influence at the temperature evolution, the gap filling influence and its thickness have been studied. The reference case has the canister-bentonite gap filled with air and the bentonite-rock filled with water.

3.1 Material gaps filling

The effect of the gap filling has been analyzed (see figure 4). It can be seen if the bentonite-rock is filled with air because of the initial design or the loss of water, the maximum temperature increases almost 5 degrees. The radiation effect has to be taken into account because of helps the heat flux. Without taken into account the radiation effect, the maximum temperature increases almost 10 degrees.

If the gap between bentonite blocks and rock is filled with pellets, a material manufactured with bentonite. The results are similar the gap filled with water. This can be expected because of the similar thermal conductivity of both materials.

3.2 Gap size

The thickness of the inner gap could increase because of the bentonite shrinkage. This case has also been analyzed (see figure 5). The mesh was modified and also the air thermal parameters in order to take into account the new gap thickness. The maximum temperature only increases in 2.5 degrees.

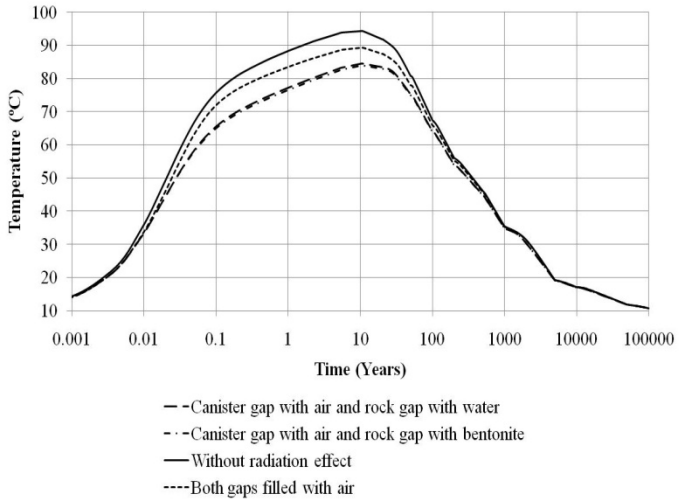

Figure 4: Material filling effect

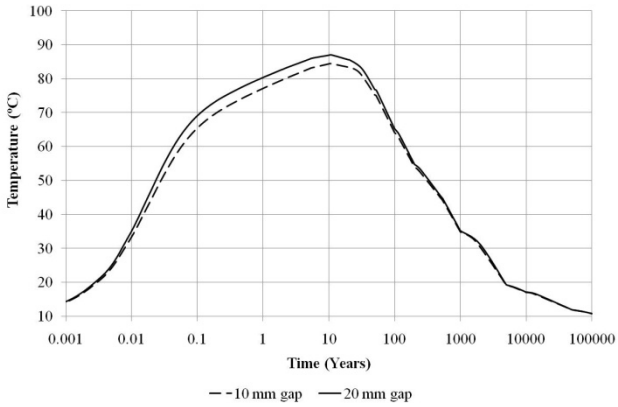

Figure 5: Gap size effect

4 CONCLUSIONS

- The maximum temperature of the canisters in the nuclear waste repository can be calculated with finite element method.
- The heat power decay from the nuclear waste has to be taken into account.
- The effect of the rest of the repository canisters can be taken into account with the analytical solution for heat sources segments in a continuous media (rock) when a single canister is studied.
- The radiation heat flux can be taken into account with the Fourier's law when the gap thickness isn't too much and the temperature difference between the two borders of the gap is small.
- The radiation flux helps to reach lower temperatures in gaps filled with air. The air has quite small thermal conductivity.
- The radiation flux depends strongly of the emissivity between the two borders of the gap.

REFERENCES

[1] Olivella, S., J. Carrera, A. Gens, E. E. Alonso, 1994a. Non-isothermal Multiphase Flow of Brine and Gas through Saline media. Transport in Porous Media, 15, 271:293

[2] Ikonen, K. (2005). Thermal Analysis of Repository for Spent EPR-type fuel. Posiva Working report 2005-06. Eurajoki.

[3] Hökmark, H., Fälth, B. (2003). Thermal dimensioning of the deep repository. SKB Technical report TR-03-09. Stockholm.

ENVIRONMENTAL ACTIONS ON SLOPE RESPONSES

S. Samat* **and J. Vaunat***

*Department of Geotechnical Engineering and Geosciences
Technical University of Catalonia (UPC)
Campus Nord UPC, 08034 Barcelona, Spain
Email: sergio.samat@upc.edu

Key words: Evaporation, Radiation, Pore Pressure, Failure

Abstract. *The paper presents different aspects of slope responses under climatic actions on the basis of the interpretation of several field cases. The interpretation is performed with the help of a general model for the coupled analysis of flow (air and water) and heat transfer in soil and rocks, including a special handling of the surface in contact with the atmosphere and the zone of vegetation roots in the soil.*

1 Introduction

Natural disasters and, more particularly landslides, are often associated to repeated climatic actions, whose consequences on geological formations and geotechnical works may be the source of important loss in terms of human life, material and economical damages. These environmental actions include all mass and heat transfer processes between the soil and the atmosphere and may have very different time scales. Current practice in evaluating the occurrence and consequences of natural disasters is based on the identification of determinant factors. Heuristic rules, statistics and probabilistic methods associated to data spatial management through Geographical Information Systems (GIS) are the methods most used to carry out the analyses. In this paper, a different approach is attempted, based on the numerical modeling of the thermo-hydro-mechanical coupled processes controlling the soil-atmosphere-vegetation exchanges on soil volumes directly imported from the GIS. Soil-atmosphere interaction is a complex phenomenon that involves balance of heat and different species (liquid water, vapour, air) across the soil surface. Such an interaction has been implemented in CODE_BRIGHT by means of a specific boundary conditions (Noilan & Planton, 1989) that impose time varying fluxes of evaporation, rainfall, radiation and heat together with changes in atmospheric pressure and temperature. Of particular relevance are the fluxes due to evaporation (E_v) and radiation (R_n) , usually

not considered in classical geotechnical applications. In this paper, the model is tested on the applications: the response of a bank to periodic infiltration, the deformation of a rock cliff under temperature changes and radiation and finally, the case of a tridimensional slope under full meteorological input (precipitations, changes in relative humidity and temperature, solar radiation and wind).

2 Numerical modeling of different field cases

The first case deals with the study of seasonal variation of pore (p_l) pressure at the upper and lower boundaries in a soft clay deposit as consequence of water level fluctuations at the creek caused by seasonal rains (one sinusoidal cycle per year). After an equilibrium interval a sinusoidal variation of liquid pressure is applied on the inclined faces (Fig1a). The attenuation of liquid pressure with depth as expected form the theory is shown in (fig.1c) (Alonso et al., 1995). Evaporation and runoff have been considered and are reflected in the response in depth of pore pressure.

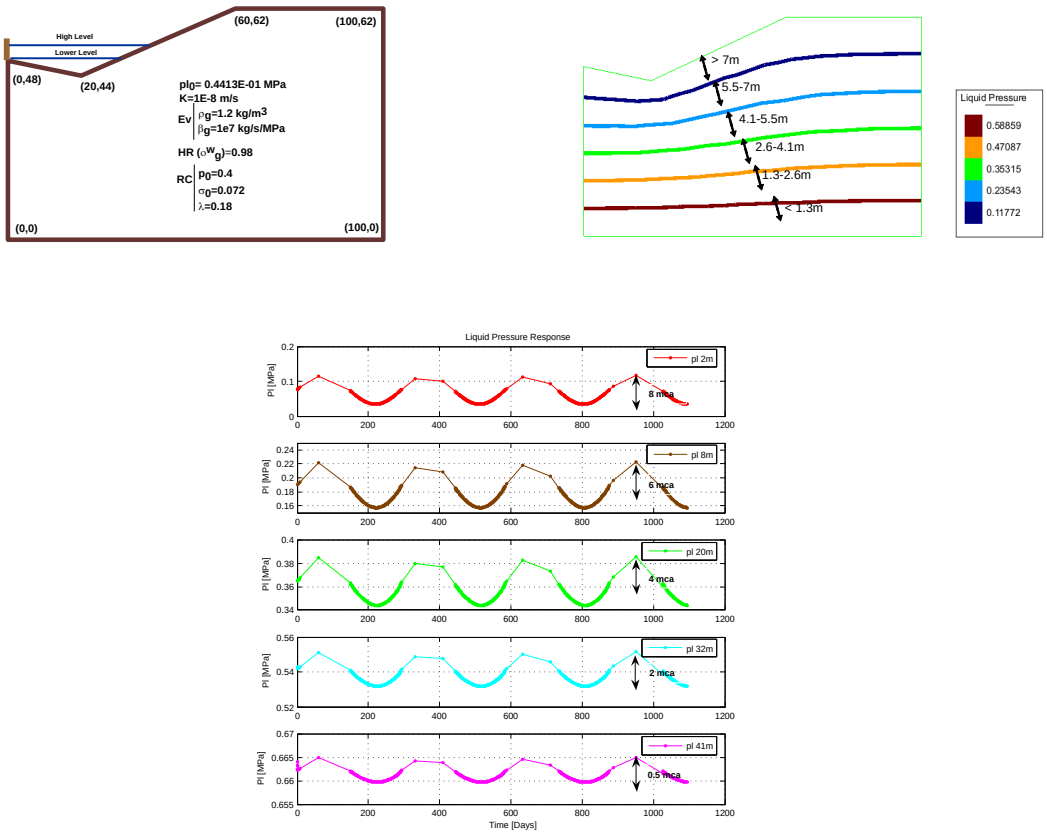

Figure 1: a)Creek and Clay Deposit Geometry and properties; b)Annual changes of Liquid pressure; c)Response of Liquid Pressure at Different Depth

The second case addresses the problem of a rock mass stability under change in temperature. The model allows to understand the temperature distribution and evolution response in the rock mass under the temperature acting at the atmosphere and the radiation (energy spread in the atmosphere). The former is obtained from the meteorological station located at the toe of the cliff, while the radiation has been simulated using the relations (1)

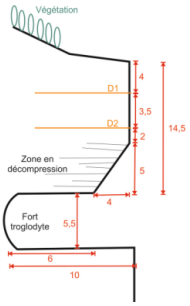

Figure 2: Rock Profile

$$R_n = (1 - A_l)\, R_g + \epsilon R_a - \epsilon \sigma T^4 \qquad (1)$$

where

$$\begin{aligned} R_a &= \sigma T_a^4 \left(0.605 + 0.048\sqrt{1370\rho_{va}}\right) \\ R_g &= \frac{\pi R_G}{2d_s} \sin\left(\frac{(t - t_m + 0.5d_s)\,\pi}{d_s}\right) \end{aligned} \qquad (2)$$

A back-analysis of the specific heat capacity and thermal conductivity of calcareous rock has been performed. Temperature profiles allow then to estimate the variation of strain in the massif.

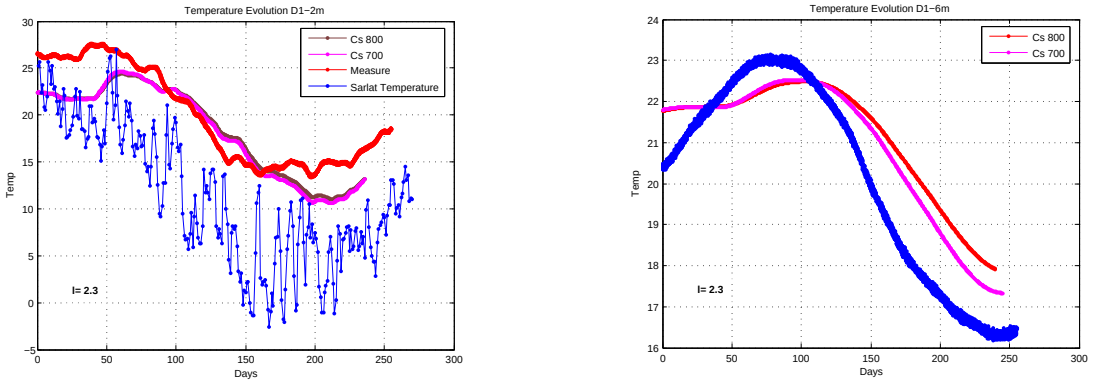

Figure 3 : a)Temp. evolution at D1; b)Temp. evolution at D2

As a third case, the response of a large hillside located at Tremp's basin (LLeida Province, Spain) is studied . The mesh has been imported in the pre-procesor **GiD** from a surface digital model. The model consists of two layers. The upper layer contains the discretization of a layer of air above the natural slope and allows for capturing the runoff on the ground. The lower layer corresponds to the soil itself. Young modulus ($E = 30$), Poisson ratio ($\nu = 0.3$) , friction angle ($\phi = 20^o$) and cohesion ($c = 0.4MPa$) have been assigned to the material. Figure (4b) shows the evolution of the effective pressure (p') as function of primary and dependent variables (p_g, S_l, p_t).

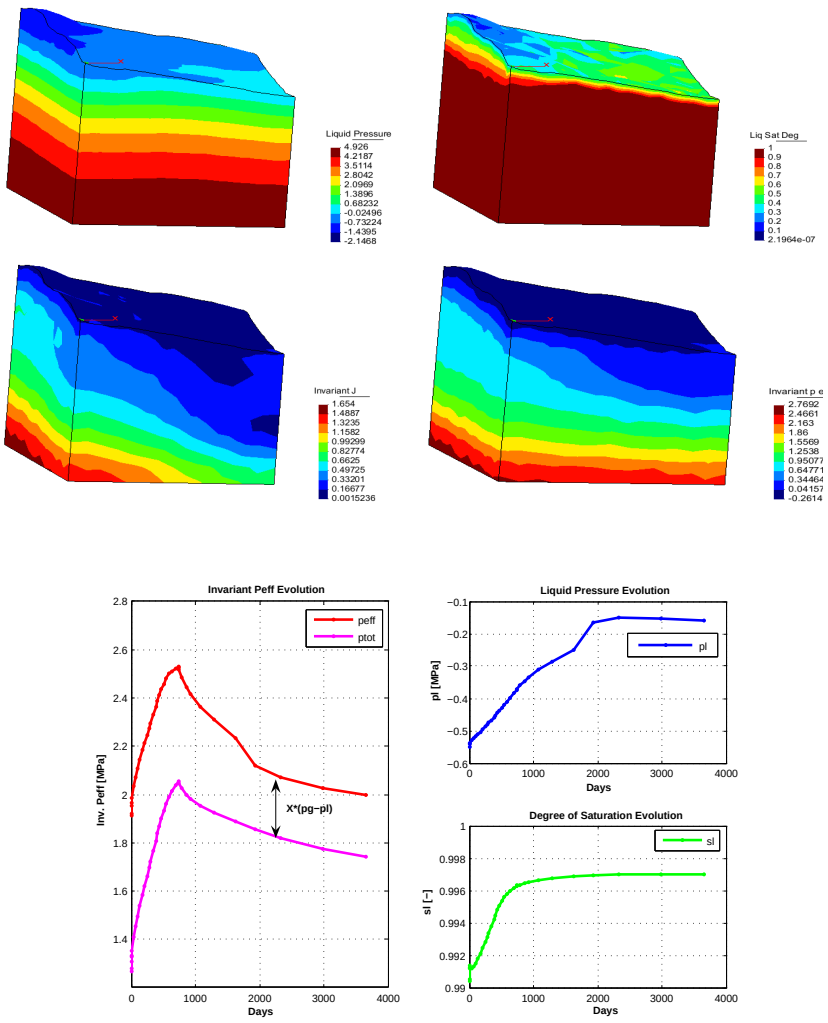

Figure 4: a)Contrours of Liquid pressure, Degree of sturation, Inv. J and Inv. p_{eff}; b)Effective and Total Pressures Evolution

CONCLUSIONS

The numerical model shows the feasibility of analyzing quantitatively three-dimensional problems of interactions soil-atmosphere by using a boundary condition specific for this process, modeling a layer to air to cope with the runoff problem and importing mesh from a surface digital model.

REFERENCES:

J.Noilan and S.Planton, 1989. A Simple Parameterization of Land Surface Processes for Meteorological Models. Monthly Weather Review, vol. 117, pp. 536-549.

Alonso,E.E., Gens, A., Lloret, A. and Delahaye, C. (1995). Effect of rain infiltration on the stability of slopes. Proc. 1st. Int. Conf. Unsaturated Soils, Paris **1**,241-248.

Fully coupled thermo-hydro-mechanical analysis for unsaturated soils in Plaxis

A. Haxaire [a], V. Galavi [a], R.B.J. Brinkgreve [b,a]

[a] *Plaxis BV, Delft, The Netherlands*

[b] *Delft University of Technology, Delft, The Netherlands*

1 INTRODUCTION

The pioneering work of the Polytechnical University of Catalonia (Olivella et al. 1994), the successful implementation of the model in the finite element method code CODE_BRIGHT (Olivella et al. 1996), the *in-situ* experiments to validate the model (Gens et al. 1998) and its implementation, and the work on the design of nuclear waste repositories (Gens et al. 2002) made it possible for THM analysis to rise and become a whole part of geomechanics.

Over the last years, the need for practical THM applications has become more and more significant, in particular for geo-environmental and geo-energy related problems. This is the reason why Plaxis started a research project on a full implementation of THM analysis.

In this paper, the governing equations of a fully coupled THM analysis are briefly described for deformable porous media. This is an extension to the previous work (Galavi et al. 2009) in which a fully coupled hydro-mechanical analysis based on Biot's consolidation theory has been developed for saturated and partially saturated soils. Here, non-isothermal partially saturated water flow, as well as heat flow, are considered. Gas pressure is assumed to be constant in the entire domain and the air flow is therefore neglected. This assumption leads to have only one independent unknown in the fluid mass balance equation which is pore water pressure. This study is based on the assumption of local thermodynamic equilibrium, meaning that all phases have the same temperature at a point of the multiphase porous medium.

In the following, the governing equations required to describe the THM model, namely water mass balance, heat transport and balance of momentum (equilibrium) equations, are described. Note that the mechanical sign convention is used, i.e. compressive stresses (in the solid and the fluid) are considered to be negative.

2 GENERAL EQUATIONS

2.1 Mass balance equation

The water mass balance can be written in the following form (Rutqvist et al., 2001):

$$n\frac{\partial}{\partial t}\left(S\rho_w+(1-S)\rho_v\right)+\left(S\rho_w+(1-S)\rho_v\right)\left[\frac{\partial \varepsilon_v}{\partial t}+\frac{(1-n)}{\rho_s}\frac{\partial \rho_s}{\partial t}\right]=-\nabla\cdot\left(\underline{J}_w+\underline{J}_v\right) \qquad (1)$$

where ρ_s, ρ_w and ρ_v are the solid, the water and the vapour densities, n is porosity, S is water saturation and ε_v is volumetric strain. $\underline{J}_w$ and $\underline{J}_v$ are the mass flux of water in water phase and in gas phase (vapour), respectively. The definition of the advective mass flux of water $\underline{J}_w$ is based on Darcy's law as:

$$\underline{J}_w=-\rho_w\left(\frac{k_{rel}}{\mu}\underline{\underline{\kappa}}^{\text{int}}\left(\nabla p_w+\rho_w\,\underline{g}\right)\right) \qquad (2)$$

where μ is the dynamic viscosity of the fluid and $\underline{\underline{\kappa}}^{int}$ is the intrinsic permeability of the porous medium. The dynamic viscosity depends on the type of fluid and temperature and the intrinsic permeability is a function of porous structure. In an unsaturated state the coefficient of permeability depends on the soil saturation. The relative permeability $k_{rel}(S)$ is defined as the ratio of the

permeability at a given saturation to the permeability in saturated state. $\underline{g} = (0, -g, 0)^T$ is the vector of gravitational acceleration. The non advective mass flux of water in gas (vapour flux), $\underline{J}_v$, is computed based on Fick's law as:

$$\underline{J}_v = -\rho_g D_v \nabla\left(\frac{\rho_v}{\rho_g}\right) \tag{3}$$

where ρ_g is the gas density and D_v is the molecular vapour diffusion coefficient in the porous media. The vapour density ρ_v is related to the temperature dependent saturated vapour density ρ_{vS} via the psychrometric law (Gens et al. 1998):

$$\rho_v = \rho_{vS} \exp\left(\frac{p_g - p_l}{\rho_w RT}\right) \tag{4}$$

where ρ_{vS} is the saturated vapour density which is the density of vapour at phreatic level, θ is the relative humidity, T is the local equilibrium temperature of the porous medium in Kelvin and p_g and p_l are gas and liquid pressures. By the assumption of atmospheric pressure, $p_w = p_g - p_l$. R is the specific gas constant for water vapour. The saturated vapour density is a temperature dependent parameter which can be obtained from empirical relationships. Here the following empirical function (Wang et al. 2009) is adopted:

$$\rho_{vS} = 10^{-3} \exp(19.891 - 4974/T) \tag{5}$$

in which ρ_{vS} is in Kg/m^3. By the assumption that the gas density is constant in Eq. (3) and substituting Eq. (4) into Eq. (3), the mass flux of water in air phase is found:

$$\underline{J}_v = -\left(D_{pv}\nabla p_w + D_{Tv}\nabla T\right) = -\left(\frac{D_v \rho_v}{\rho_w RT}\nabla p_w + f_{Tv} D_v\left(\theta\frac{\partial \rho_{vS}}{\partial T} - \frac{\rho_v p_w}{\rho_w RT^2}\right)\nabla T\right) \tag{6}$$

f_{Tv} is a thermal diffusion factor which is introduced to control effect of temperature on the non-advective water mass flux. By expanding Eq. (1), the water mass balance equation is derived:

$$\begin{aligned}
&\left[n(\rho_w - \rho_v)\frac{\partial S}{\partial p_w} - nS\rho_w\beta_{wP0} - n(1-S)\frac{\rho_v}{\rho_w RT}\right]\frac{\partial p_w}{\partial t} \\
&+\left[n(\rho_w - \rho_v)\frac{\partial S}{\partial T} - nS\rho_w\beta_{wT0} + n(1-S)\left(\theta\frac{\partial \rho_{vS}}{\partial T} - \frac{\rho_v p_w}{\rho_w RT^2}\right)\right]\frac{\partial T}{\partial t} \\
&-\left[(S\rho_w + (1-S)\rho_v)(1-n)\beta_{sT}\right]\frac{\partial T}{\partial t} \\
&+(S\rho_w + (1-S)\rho_v)\frac{\partial \varepsilon_v}{\partial t} + \nabla\cdot(\underline{J}_w + \underline{J}_v) = 0
\end{aligned} \tag{7}$$

where β_{wP0} and β_{wT0} are the reference compressibility and volumetric thermal expansion of water. The volumetric thermal expansion of water at 293.15 K is 2.1×10^{-4} (1/K). β_{sT} is the volumetric thermal expansion coefficient of soil grains.

2.2 Balance of momentum

For a representative elemental volume of the soil the linear momentum balance is given by:

$$\nabla\cdot(\underline{\sigma}) + ((1-n)\rho_s + nS\rho_w)\underline{g} = \underline{0} \tag{8}$$

In Eq. (9) $\underline{\sigma}$ is the well-known Bishop stress (Bishop & Blight, 1963):

$$\underline{\sigma} = \underline{\sigma'} + \left(\chi p_w + (1-\chi) p_g\right)\underline{m} \tag{9}$$

where $\underline{m} = (1,1,1,0,0,0)^T$ is the identity vector and χ is an experimentally determined factor which depends on the degree of saturation, the porosity, and the matrix suction. As the pore gas pressure is assumed to be constant and equal to the atmospheric pressure, the pore gas pressure can be neglected. Therefore the Bishop's stress (average stress) can be simplified as:

$$\underline{\sigma} = \underline{\sigma'} + \chi p_w \underline{m} \tag{10}$$

The constitutive relation using the effective stress $\underline{\sigma'}$ is written in the following form:

$$d\underline{\sigma'} = \underline{\underline{M}}\left(d\underline{\varepsilon} - d\underline{\varepsilon}_T\right) \tag{11}$$

$\underline{\underline{M}}$ represents the material stress-strain matrix. $\underline{\varepsilon}$ is the total strain of the skeleton and $\underline{\varepsilon}_T$ is thermal strain caused by temperature increase. The thermal strain can be found from:

$$d\underline{\varepsilon}_T = \underline{\underline{B}}_{DT} \cdot \underline{m} \cdot dT = (\beta_{DT,x}, \beta_{DT,y}, \beta_{DT,z}, 0,0,0)^T \cdot dT \tag{12}$$

where $\beta_{DT,x}$, $\beta_{DT,y}$ and $\beta_{DT,z}$ are the drained linear thermal expansion coefficient of soil skeleton (1/K) in x, y and z directions, respectively. Khalili et al. (2010) showed that the thermal expansion coefficient of soils grains is the same as the skeletal thermal expansion coefficient of homogenous porous media. Therefore $\beta_{sT} = \beta_{DT,x} + \beta_{DT,y} + \beta_{DT,z}$. The constitutive relation (11) can be written as:

$$d\underline{\sigma'} = \underline{\underline{M}}\left(d\underline{\varepsilon} - \underline{\underline{B}}_{DT}\underline{m} \cdot dT\right) \tag{13}$$

The governing equation for the deformation model is then obtained:

$$\nabla \cdot \left[\underline{\underline{M}}\left(d\underline{\varepsilon} - \underline{\underline{B}}_{DT}\underline{m} \cdot dT\right) + \chi\, dp_w\, \underline{m}\right] + d\left(\rho \underline{g}\right) = 0 \tag{14}$$

2.3 Heat transport

The heat balance equation for the porous medium can be written in the following form:

$$C\rho \frac{\partial T}{\partial t} = \nabla \cdot \left(\underline{J}_c + \underline{J}_{Aw}\right) + Q_T \tag{15}$$

in which $\underline{J}_{Aw}$ and $\underline{J}_c$ are the advective internal energy flux in water and the conductive heat flux in the porous medium, respectively. Q_T is the heat source term, i.e. heat generation rate per unit volume. $C\rho$ is the heat capacity of the porous medium:

$$C\rho = (1-n)C_s\rho_s + nSC_w\rho_w + n(1-S)C_v\rho_v \tag{16}$$

where C_s, C_w and C_g are the solid, the water and the gas specific heat capacities. The conductive heat flow is assumed to be governed by Fourier's law:

$$\underline{J}_c = -\lambda \nabla T \tag{17}$$

where λ is the averaged thermal conductivity of the porous medium:

$$\lambda = (1-n)\lambda_s + nS\lambda_w + n(1-S)\lambda_v \tag{18}$$

where λ_s, λ_w and λ_g are the solid, the water and the gas thermal conductivities. The advective internal energy flux in water is:

$$\underline{J}_{Aw} = C_w T \underline{J}_w = -\rho_w C_w T \left(\frac{k_{rel}}{\mu} \underline{\underline{\kappa}}^{\text{int}} (\nabla p_w + \rho_w \underline{g}) \right) \tag{19}$$

By expanding Eq. (15) and considering air temperature at the ground surface as boundary conditions, the governing equation on heat transport can therefore be written as:

$$\begin{aligned} & C\rho \frac{\partial T}{\partial t} + \nabla \cdot (\lambda \nabla T) + \rho_w C_w \left[\frac{k_{rel}}{\mu} \underline{\underline{\kappa}}^{\text{int}} (\nabla p_w + \rho_w \underline{g}) \right] \cdot \nabla T \\ & + \rho_w C_w T \left[\nabla \cdot \left(\frac{k_{rel}}{\mu} \underline{\underline{\kappa}}^{\text{int}} (\nabla p_w + \rho_w \underline{g}) \right) \right] - Q_T + C_{as} (T - T_a) = 0 \end{aligned} \tag{20}$$

where T_a is the air temperature and C_{as} (W/m^{2}K) is the convective heat transfer coefficient at the surface in contact with air.

3 CONCLUSION

The constitutive model presented in this paper brings the possibility to model THM phenomena in Plaxis. Although being still a research project, this implementation becomes more and more mature and will soon allow its use for practical applications.

REFERENCES

Bishop, A.W., Blight, A.K.G. (1963) Some aspects of effective stress in saturated and partially saturated soils. Géotechnique, 13, 177-197.

Galavi, V., Brinkgreve, R.B.J., Bonnier, P.G., Gonzalez, N.A. (2009) Fully coupled hydro-mechanical analysis of unsaturated soils. Proceedings of the 1st symposium on computational geomechanics (COMGEO I), Juan-les-Pins, Francs, 29 April-1 May.

Gens, A., Guimaraes, L. d. N., Garcia-Molina, A., Alonso, E. (2002) Factors controlling rock-clay buffer interaction in a radioactive waste repository. Engineering Geology, 2002, 61, 297-308

Gens, A.; Garcia-Molina, A.J.; Olivella, S.; Alonso, E.E. & Huertas, F. (1998) Analysis of full scale *in situ* test simulating repository conditions. Int. J. Numer. Anal. Meth. Geomech., 22, 515-548.

Khalili, N., Uchaipichat, A., Javadi, A. (2010) Skeletal themal expansion coefficient and thermo -hydro-mechanical constitutive relations for saturated homogeneous porous media. Mechanics of Materials, 42, 593-598.

Olivella, S., Carrera J., Gens A., Alonso E.E. (1994) Non-isothermal multiphase flow of brine and gas thorough saline media, Transport in Porous Media, 15, 271-293.

Olivella, S., Gens, A., Carrera, J., Alonso, E.E. (1996) Numerical formulation for a simulator (CODE_BRIGHT) for the coupled analysis of saline media. Engineering Computations, 37, 87-112.

Rutqvist, J., Borgesson, L., Chijmatsu, M., Nguyen, T.S., Jing, L., Noorishad, J., Tsang, C.-F. (2001) Coupled thermo-hydro-mechanical analysis of a heater test in fractured rock and bentonite at Kamaishi Mine - Comparison of field results to predictions of four finite element codes. International Journal of Rock Mechanics & Mining Sciences, 38, 129-142.

Wang, W., Kosakowski, G., Kolditz, O. (2009) A parallel finite element scheme for thermo-hydro-mechanical (THM) coupled problems in porous media Computers & Geosciences,35, 1631-1641.

AN ANALYSIS TOOL FOR INVESTIGATING THE PERFORMANCE OF CODE_BRIGHT SIMULATIONS

Ola Kristensson[*] and Daniel Malmberg[*]

[*] Clay Technology AB
IDEON Research Center
S-223 70 Lund, Sweden
e-mail: osk@claytech.se

Key words: Simulation analysis tool, convergence

Abstract. *A tool to analyze the convergence of CODE_BRIGHT simulations has been developed. The information given in the simulations information file (name_gen.out,) is read and the data in it processed, where after output files are generated. The data can then easily be visualized in, for example, Microsoft Excel. This allows the user to analyze how the convergence has evolved in terms of "governing" indicators such as; processes (THMG) and residuals (balance and/or variable). Also, the nodes where the "difficulties" occur are identified. In addition, an output file is generated such that the time-evolution of the "convergence indicators" may be visualized directly on the model geometry using GiD.*

1 INTRODUCTION

When solving problems with CODE_BRIGHT it is often quite difficult to quickly get a picture of the performance of the code. The information about the simulation is given in a text file (*name_gen.out*) where time-step size, as well as balance and variable residuals, are given. If the model is complex, either in terms of the total number of degrees of freedom or in the number of active processes modeled (Thermal (T), Hydraulic (H), Mechanical (M) and Gas (G)), it can be a rather time consuming task to get an overview of the state of the simulation when reading *name_gen.out.* Furthermore, this file can grow very large, making it almost impossible to analyze it directly in a plotting program or text editor.

To facilitate a more rapid establishment of the convergence state of the simulation, a small analysis tool has been developed, where information is extracted from *name_gen.out* and written to smaller output files. The information in these files may easily be visualized using plot programs where 3D-data can be managed (e.g. Excel). Furthermore, information is written to another file in a format that GiD can import and the convergence information may therefore also be visualized directly on the model geometry (to do this it also necessary create a copy of the original ASCII mesh file with a somewhat modified name).

Below, the analysis tool is described, and the required input as well as the currently available output is listed. Thereafter follows two examples, where the tool has been used to analyze the output from 1) a large hydraulic 3D-model, and 2) a fully coupled THMG model.

2 WORKING PRINICIPLE, INPUT AND OUTPUT

The working principle is rather straightforward. The *name_gen.out* file is read line by line, and when certain keywords are identified information is read and different actions takes place depending on the keyword. If data is to be operated on, or saved for later usage, it is stored in

arrays. Other data is simply written directly to a "streamlined" output file to facilitate plotting.

The required input data is:

- the name of the model (substituted by the label *name* in these notes) to be analyzed. Either by providing a *root.dat* file, or, if this does not exist, by keyboard input.
- a *name_gen.out* file corresponding to the model-name given.
- which of the active processes (T, H, M & G), that should be evaluated
- selection of optional output
- a start and an end time between which the simulation is evaluated (see Figure 1)
- length of the time intervals for which output is given (see Figure 1). Defined by a fraction of the evaluation time.
- number of time intervals, $\geq (t_{end}^{eval} - t_{end}^{eval})/ t_{interval}^{eval}$ since the intervals may overlap.

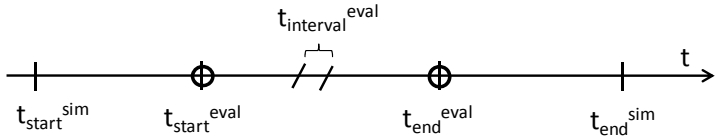

Figure 1: Representation of the time related input.

The standard output (always given) is:

- on screen (for the whole simulation):
  - number of time steps (*ntime*)
  - number of time increments (*ndtime*)
  - number of Newton-Raphson iterations (*nNR*)
  - number of Newton-Raphson iterations within time increments that did not converge (*wastedNR*)
  - ntime/ndtime: indicating efficiency
  - (*nNR-wastedNR*)/*nNR*: indicating efficiency
- {*time*, *dtime*, number of NR iteration within dtime} given in *iter_name.out*
- the information described in item (1.) below (in the optional output description), but here in GiD-format. This data is saved to the file *THMG_name.out*, which should be loaded together with an ASCII mesh-file named *THMG_name.msh* in GiD.

The optional output is:

1. {*time*, *node*, *frequency*} in the files *X_Y_name_gen.out* where:
   - *time* is the mid-time of the currently evaluated time interval,
   - *node is* the nodes where convergence occurred in the last NR-iteration for all time increments, within the currently evaluated time interval, and
   - *frequency is* the number of times the node converges in the last NR-iteration, within the currently evaluated time interval.

   In the file names, *X* is substituted with either T, H, M or G, to identify the process in question, and *Y* is substituted with either bal (for balance residual) or var (for variable residual) respectively.

2. {*time*, *process*, *frequency*} in the file *process_name_gen.out* where:
    - *time* is the mid-time of the currently evaluated time interval
    - *process* = {*A* – 1: if balance residual, *A* + 1: if variable residual} where *A* = {10: if T, 20: if H, 30: if M, 40: if G}. This is an indicator of the process/processes and the type of residual (balance and/or variable) for which convergence occurred in the last NR-iteration for all time increments within the currently evaluated time interval.
    - *Frequency* is the sum of the node frequencies for the process.

3 ANALYSING A LARGE HYDRAULIC 3D-MODEL

Here the numerical performance of CODE_BRIGHT is analyzed for a large (33747 nodes) and purely hydraulic 3D-model, using the developed tool. The start time, end time, time-interval size and number of intervals are; 101 days, 179 days, 0.005 and 200, respectively. As can be seen below in Figure 2, where *H_var_name_gen.out* has been imported into Excel and plotted as a bubble diagram, the frequency (the number of times a given node converges in the last NR-iteration during the analyzed time interval), indicated by the bubble size, is highest in a few nodes with numbers slightly below 5000, during the evaluated time range.

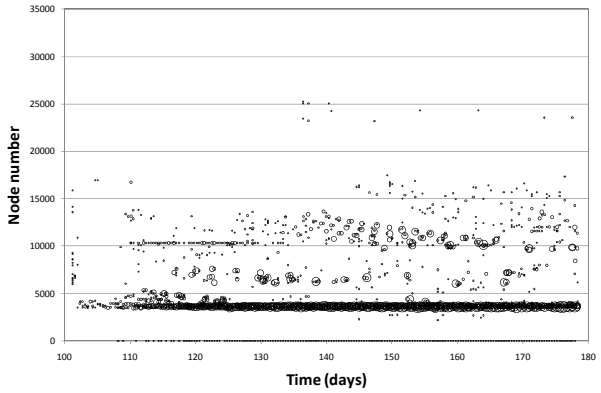

Figure 2: Analysis of the governing nodes given in *H_var_name_gen.out*.

When importing *THMG_name.out* together with *THMG_name.msh* into GiD and selecting to show the "H var" variable as a vector plot (here the "y-element" has been selected), the visualization shown in Figure 3 is obtained. In Figure 3 the end of the vector identifies the node and the length of the vector corresponds to the frequency of that node in the time interval selected. The result is shown for two time intervals and indicates that it is hard to obtain convergence in the rock surrounding the bottom part of the left nuclear-waste canister.

4 ANALYSING A THMG-MODEL

The second model analyzed is an axisymmetric THMG-model. When importing *process_name_gen.out* into Excel and again plotting the data in a bubble chart, the graph shown to the left in Figure 4 is obtained. It can be seen that the dominating process governing the convergence during the simulation is "H var" which also show the largest frequency at the very end of the simulation. At some occasions also "T bal" and "M bal" is converging in the very last NR-iteration within the time step.

If *H_var_name_gen.out* is imported into Excel in the same way as before (shown to the right in Figure 4), it can be seen that during the simulation the largest difficulties, in terms of convergence, occurs at nodes 101 and 102 (where a boundary condition is prescribed). At the very end of the simulation, however, the difficulties occur around node 65.

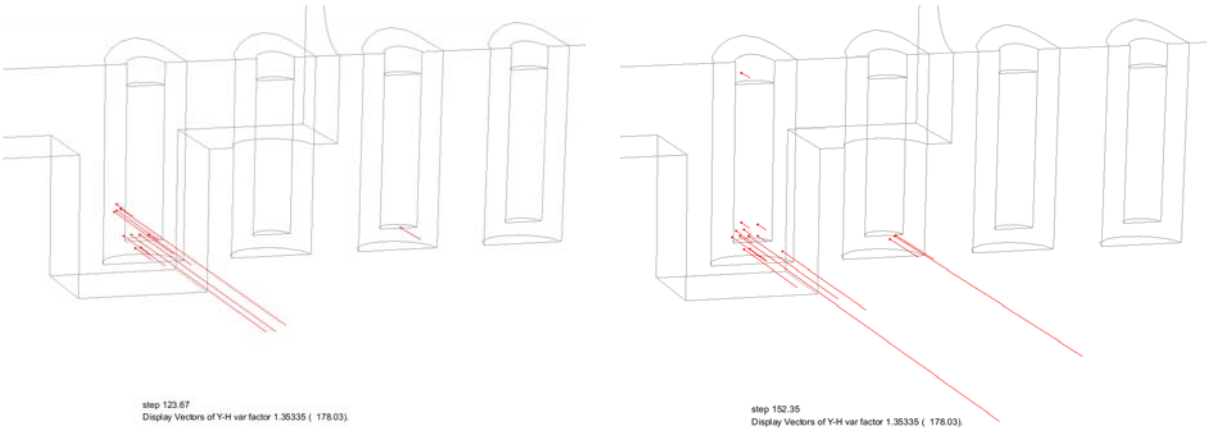

Figure 3: The information in *THMG_name.out* visualized in GiD at two times.

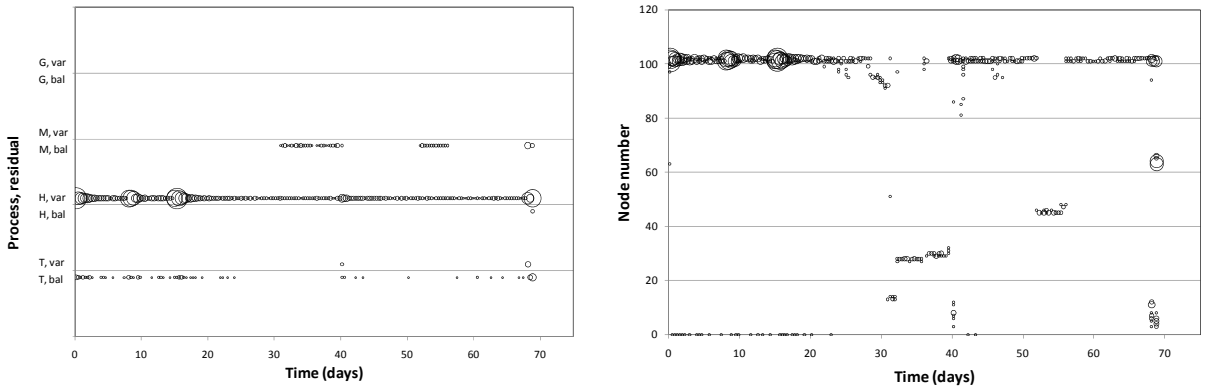

Figure 4: Analysis of the governing processes given in *process_name_gen.out* (left) and analysis of the governing nodes given in *H_var_name_gen.out* (right).

5 CONCLUSIONS

The developed analysis tool increases the possibility of quickly finding out which process/processes cause problems in convergence in a given CODE_BRIGHT simulation, and also helps in locating where on the geometry these problems occur. Since the indication-parameter for convergence difficulties (frequency) is calculated in a given number of intervals, rather than for each time step, the data files to visualize becomes manageable. Output from the tool comes in form of text files easily imported into some visualization program (e.g. Excel) and a file, which together with a renamed mesh file, can be imported into GiD, where the location and frequency are visualized on the model geometry.

BARCELONA EXPANSIVE MODEL IN CODE_BRIGHT: IMPLEMENTATION AND PERFORMANCE

J. Vaunat; N. Pinyol; A. Sant; E. Alonso; A. Gens; N. González

Department of Geotechnical Engineering and Geosciences
Technical University of Catalonia (UPC)
Campus Nord UPC, Módulo D2, 08034 Barcelona, Spain
jean.vaunat@upc.edu; nuria.pinyol@upc.edu; alexandre.sant@upc.edu;
eduardo.alonso@upc.edu; antonio.gens@upc.edu; nubia.aurora.gonzalez@upc.edu

Keywords: Bentonite, swelling clays, hydro-mechanical coupling, Barcelona expansive model, double-structure.

Abstract: The Barcelona Expansive Model is briefly presented and its performance within the Finite Element program CODE_BRIGHT analyzed. Two applications are considered: the response of compacted samples of low plasticity silt during wetting, the synthetic case of swelling seal in a gallery.

1 INTRODUCTION

Gens and Alonso (1992) presented a conceptual basis to model expansive soils in which two distinct levels of structure are distinguished: the microstructural level at which swelling of active minerals takes place and the macrostructural level responsible for major structural rearrangement. Designed to model the response of expansive clays, the Barcelona Expansive has proved to reproduce important features of expansive soils, such as: dependency of swelling pressure and swelling strain on initial dry density and water content, collapse followed by swelling during swelling pressure, macropores invasion by microstructure, macropores generation during strong drying, accumulation of plastic strain during suction cycles. In this paper, the use of Barcelona Expansive Model in the framework of boundary values problems is presented.

2 BARCELONA EXPANSIVE MODEL

The following assumptions are adopted:

1. The microstructural behaviour is elastic and volumetric and controlled by the effective stress;
2. Mechanical, hydraulic and chemical equilibrium exists between microstructure and macrostructure;
3. Coupling between microstructure and macrostructure results in possible macrostructural elastoplastic strains when elastic microstructural strains take place.

Mathematical formulation considers the following ingredients:

1. The microstructural volumetric strain is related to the microscopic effective stress $\hat{p} = p + S_r^{\alpha} s$ by the relationship $\mathrm{d}\varepsilon_{vm}^{e} = \dfrac{\mathrm{d}\hat{p}}{K_m}$ with $K_m = \dfrac{e^{-\alpha_m \hat{p}}}{\beta_m}$ or $K_m = \dfrac{(1+e_m)\hat{p}}{\kappa_m}$, where S_r is the degree of saturation of the microstructure, K_m the bulk modulus of the microstructure, e_m the void ratio of the microstructure, α, α_m, β_m and κ_m material parameters.
2. The microstructural elastic strain is related to the mean net stress by $\mathrm{d}\varepsilon_{vM}^{e} = \dfrac{\mathrm{d}p}{K_t} + \dfrac{\mathrm{d}s}{K_s}$ with $K_t = \dfrac{(1+e_M)p}{\kappa}$ and $K_s = \dfrac{(1+e_M)(s+p_{atm})}{\kappa_s}$, where K_t and K_s are, respectively,

the bulk moduli of the macrostructure against stress and suction changes, e_M is the macrostructural void ratio, p_{atm} a reference pressure (usually atmospheric) and κ and κ_s two material parameters.

3. When the yield loci drawn in Figure 1 are reached, plastic strains develop. LC yield surface define the onset of macrostructural plastic strain due to loading of collapse. They read: $d\varepsilon_{vM}^{p} = \frac{\lambda - \kappa}{1 + e_M} \frac{dp_0}{p_0}$, where λ and κ are, respectively, the plastic and elastic stiffness parameter and p_0 the isotropic yield point. SI and SD yield surface define the onset of macrostructural volumetric plastic strain caused by the swelling/shrinkage of microstructure. Ratio of macrostructural over microstructural strain is related to the state of density of the sample by the coupling functions f drawn in Figure 1.b (f_I applies to drying – suction increase –and f_D to wetting – suction decrease – processes). State of density is expressed by the ratio of the current mean net stress over the isotropic yield point.

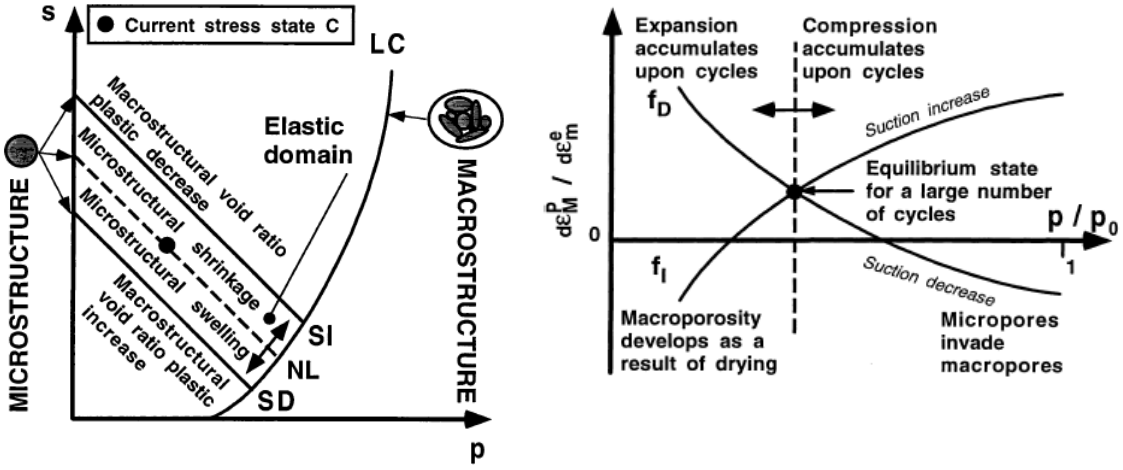

a) b)

Figure 1: Main features of Barcelona Expansive Model: a) yield loci in p-s plane; b) coupling functions between microstructural strain and macrostructural plastic strain (after Alonso et al., 1999)

3 RESPONSE OF COMPACTED LOW PLASTICITY SILT UNDER WETTING.

Volume changes of compacted soils upon saturation depend mainly on the initial compaction water content, dry density and the applied stress at the time of wetting. Often, the results are plotted as contour maps of induced volumetric strains during saturation in the Proctor space. This is the case of the results shown in Figure 9. Statically compacted samples of a low plasticity silty clay from Barcelona (w_L = 30.5, PI = 11.8) were saturated under loading in a conventional oedometer apparatus. The values plotted indicate the expansive (negative sign) and collapse (positive sign) strains measured during wetting. From these results, it can be concluded that collapse takes place in low densities samples whereas swelling is associated to denser samples. There is an intermediate density which shows no volumetric strains during wetting.

The elastoplastic double structure model is used to capture the response of compacted soils taking into account the mentioned initial compaction conditions. The list of the constitutive parameters of the model and a short description of them are indicated in Table 1. The computed results in terms of volumetric strains observed during the wetting stage are plotted in Figure 13. The model is capable of reproducing

wetting induced collapse or swelling behaviour depending on the initial preconsolidation state.

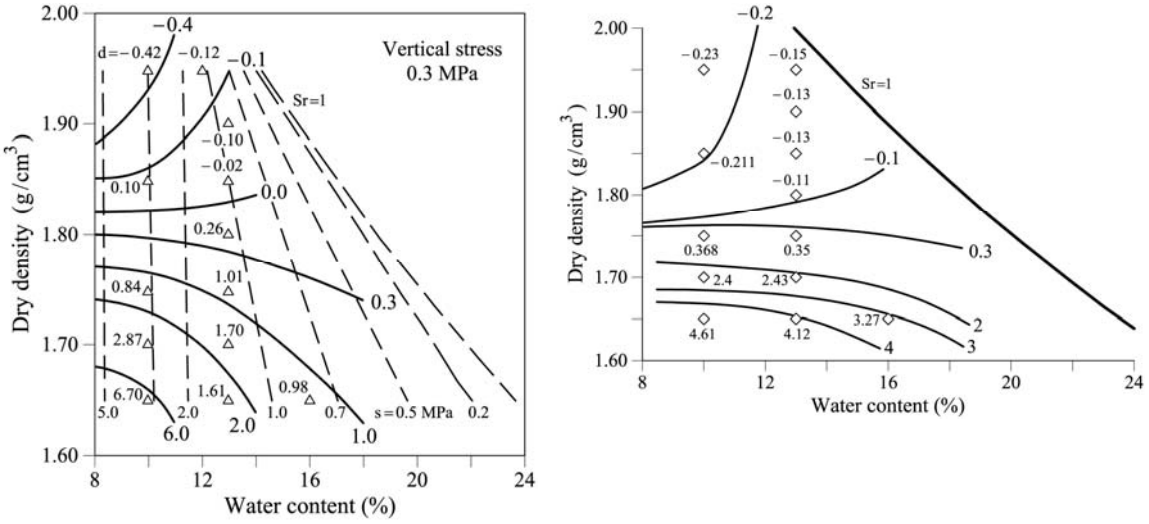

Figure 2: Changes in density during wetting: a) experimental and b) numerical results (after Pinyol & Alonso, 2011)

Symbol	Definition of parameter	Value
ν_M	Matrix Poisson's ratio	0.3
κ	Elastic macro stiffness parameter for changes in net mean stress	0.003
κ_s	Elastic macro stiffness parameter for changes in suction	0.001
κ_m	Elastic micro stiffness parameter for changes in effective mean stress	0.001
$\lambda(0)$	Macro stiffness parameter for virgin states under saturated conditions	0.055
r, β	Parameters that describe the rate of changes of virgin compressibility parameter with macro suction	0.75,1 MPa^{-1}
M	Slope of critical-state line	1.2 MPa
k_s	Parameter that controls the increase of cohesion with suction	0
p_c	Reference stress	0.001 MPa
f_{I0}, f_{I1}, n_I	Parameters micro-macro for coupling functions when SI is active	-1, 5, 0.6
f_{D0}, f_{D1}, n_D	Parameters micro-macro for coupling functions when SD is active	1, 5, 2

Table 1 : Barcelona Expansive Model parameters

4 RESPONSE OF A BENTONITE SEAL

To assess the performance of the model within a boundary value problem, the synthetic case of a bentonite seal of 5 meter long and diameter 2.2 m is considered. Material parameters are given in Table 2. Geometry and mesh in Figure 3. Normal displacements are restricted at the boundaries of the seal. An artificial hydration starts at day 0 and ends when the bentonite reaches saturation. Saturation is modeled by applying a small liquid pressure (0.1 MPa) on 6 filters within the seal.

Results of displacements at different times during the hydration are plotted in Fig. 3 and Fig. 4. The dissymmetry in water injection makes a non homogeneous swelling of the seal at early times. Activation of SI and SD yield surfaces, accompanied by permanent irreversible strain, makes that the distribution of the density within the seal keeps the memory of the non homogeneity at full saturation.

Hydraulic and thermal data				
Retention Curve: ITYCL=1 (Van Genutchen Model)				
P1	P_0	15	MPa	
P2	σ_0	0.072	N*m-1	
P3	λ	0.29		
P4	S_rl	0.15		
P5	S_ls	1		
Intrinsic Permeability: ITYCL=1 (Kozeny's model)				
P1	k11_0	1.0E-18	m2	
P2	k22_0	1.0E-18	m2	
P3	k33_0	1.0E-18	m2	
P4	ϕ_0	0.35		
P5	ϕ_min	0.01		
Liquid Phase Rel. Permeability: ITYCL=6 (Generalised power)				
P2	A	1		
P3	λ	3		
P4	S_rl	0.15		
P5	S_ls	1		

Mechanical data for BXM			
ICL70, ITYCL = 0 NO BONDED STRUCTURE IS CONSIDERED			
ICL71, ITYCL = 4 ELASTIC MODEL			
P1	κ_macro	0.03	MPa
P2	κ_micro	0.008	MPa
P5	κs_macro	0.007	MPa
P6	ν	0.2	
P7	Mín K_macro	1	MPa
P8	Mín K_micro	1	MPa
ICL72, ITYCL = 4 COUPLING BEHAVIOUR			
P1	χ_0	0	
P2	c_b	0	
P3	f_sd_0	0.1	
P4	f_sd_1	0	
P5	n_sd	2	
P6	f_sd_0	0	
P7	f_sd_1	0.1	
P8	n_si	0.5	

ICL73, ITYCL = 4 BBM for the clay matrix-shape p/q diagram			
P1	M	1	
P3	r	0.8	
P4	β	0.1	MPa-1
P5	pc	0.1	MPa
P6	ks	0.1	
P7	ps	0.1	MPa
ICL75, ITYCL = 4 BBM plastic potential for the clay matrix			
P1	ω	1	associative plasticity
ICL77, ITYCL = 4 BBM hardening law for the clay matrix			
P1	λ(0)	0.2	
ICL79, ITYCL = 4 Control parameter for the S.P.A.			
P1	tol	1.00E-08	
P2	itmax	30	
P3	isubmax	500	
P4	iJac	-1	
P8	P_atm	0.1	Mpa

Table 2 : Material parameters

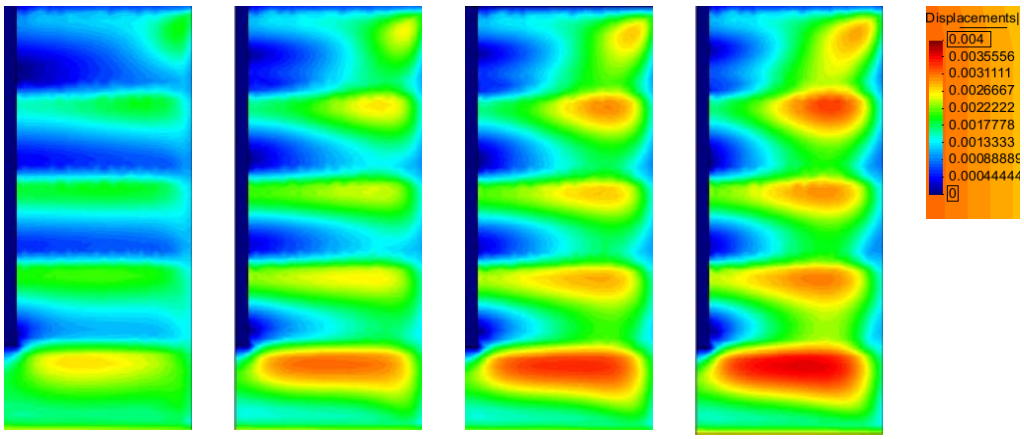

t = 1 d t = 3 d t = 5 d t = 11 d

Figure 3: Isochrones of displacement (m) in the enclosure for different times of the analysis.

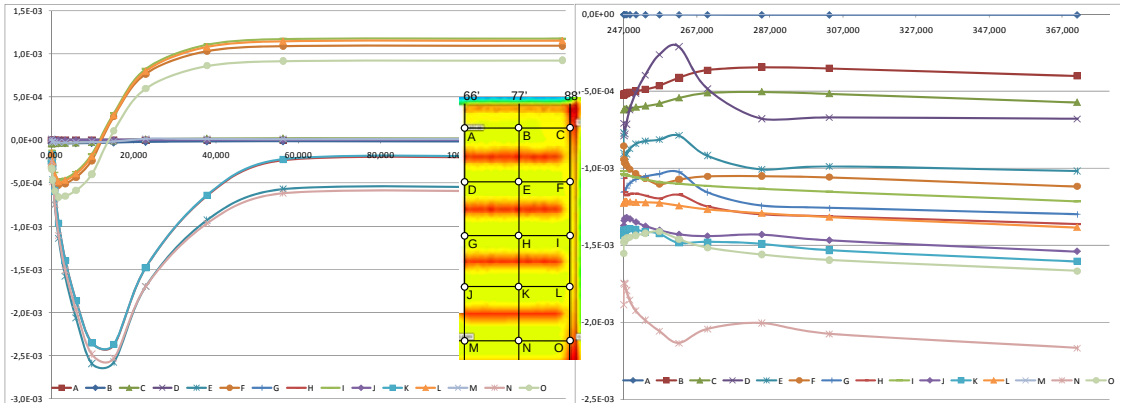

Figure 4 : Evolution of radial displacements at different points within the seal.

REFERENCES

Alonso, E.E., Vaunat, J. and A. Gens, 1999. Modelling the mechanical behavisour of expansive clays. *Engineering Geology*, **54,** 173-183, Elsevier Applied Science.

Gens, A. and E.E. Alonso, 1992. A framework for the behaviour of unsaturated expansive clays. *Canadian Geotechnical Journal*, **29**, 1013-1032.

Pinyol, N.M. and E. Alonso, 2011. Modelling compacted soils. *6th International conference on dam engineering*, Lisbon, Portugal, February 15-17, 2011.

THE STRUCTURE OF CODE-BRIGHT: FLOWCHART AND FUTURE DEVELOPMENTS

José M. Gesto[*], Nubia A. González[*], Sebastià Olivella[*], Jean Vaunat[*] and Antonio Gens[*]

[*] Department of Geotechnical Engineering and Geosciences
Technical University of Catalonia (UPC)
Campus Norte UPC, 08034 Barcelona, Spain
e-mail: jose.manuel.gesto@upc.edu, nubia.aurora.gonzalez@upc.edu, sebastia.olivella@upc.edu, jean.vaunat@upc.edu, antonio.gens@upc.edu,
web page: http://www.etcg.upc.edu/research/code_bright/

Key words: CODE-BRIGHT, FlowChart.

Abstract. *In this work we present and describe the main features of a flowchart for the version v3beta of CODE-BRIGHT that has been prepared in EXCEL with the aim that it may be a useful tool for users and programmers. We also talk about some new developments that are to be carried out regarding the basic structure of CODE-BRIGHT.*

1 INTRODUCTION

CODE-BRIGHT (COupled DEformation BRIne, Gas and Heat Transport) is a Finite Element Program created by the Department of Geotechnical Engineering and Geosciences of the Universidad Politècnica de Catalunya. The program was initially developed more than fifteen years ago on the basis of a new general theory for saline media[i]. Since then, the program has been generalized for modeling thermo-hydro-mechanical (THM) processes in a coupled way in geological media, and also the coupled effects of chemical phenomena have been included in some versions of the program.

In the last years, CODE-BRIGHT has been used for modeling many complex interaction problems[ii], and the number of programmers, sponsors and users has experienced a considerable increase. The source code of the current version v3beta of CODE-BRIGHT[iii] consists of more than forty files written in FORTRAN that contain more than four hundred subroutines and twenty-five functions. The high quantity of files and subroutines, as well as the presence of modules created by different programmers with different purposes and with different versions of FORTRAN, often make new users and programmers to find difficulties for the implementation of their desired models or, in general, for performing modifications in the program. In order to ease the global understanding of the structure of the program and provide users and programmers with a tool to visualize the connections between the different parts of it, a flowchart of CODE-BRIGHT has been worked out. In this paper we describe the basic features of this flowchart and we present the future developments that are to be realized regarding the global structure of CODE-BRIGHT.

2 THE FLOWCHART

An EXCEL file has been created whose different sheets contain registers of the subroutines and functions included in each one of the files that compose the CODE-BRIGHT FORTRAN

Project, a list of variables used in the program with the description of their main properties (dimensions, type of variable, comments, etc.), a list of units for reading and writing and, finally, a flowchart of the program. The flowchart displays the text of the program in such a way that the position of the cells, their color, the text inside and the attached comments provide the reader with information about its structure.

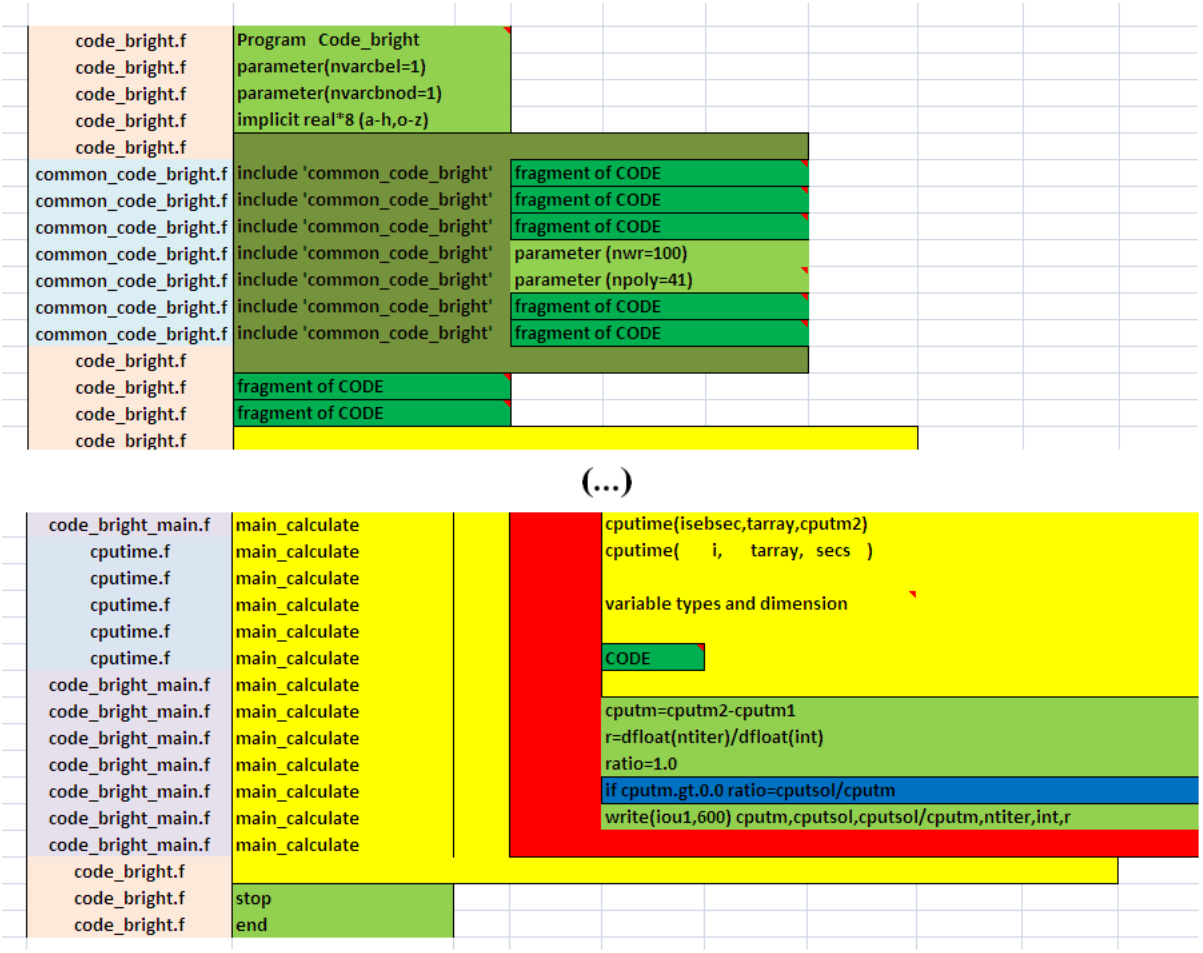

Figure 1: Organization of the cells (beginning and ending of the flowchart)

2.1 Organization of the cells

The cells placed more to the right in each row of the flowchart (or their attached comments, see Subsection 2.3) contain lines or fragments of CODE-BRIGHT (Figure 1). Reading the rows from top to bottom, one can follow the fragments in the order they are executed when CODE-BRIGHT runs. The cells of the first column of the flowchart indicate the file that contains the corresponding line or fragment of the program. When some remarkable event takes place (a subroutine is called, a loop or a logical condition starts, etc.), the cells that contain the text of the program are displaced to the right until the event finishes (the subroutine returns to the original file, the loop or the logical condition finishes, etc.). In this way, it is easy to know the number of openings of loops and logical conditions, subroutine callings, etc., that precede each fragment of the program (Figures 1 and 2).

When a subroutine is called, the list of local arguments is displayed below the cell that

contains the arguments in the calling command, so it results straightforward to see the correspondence between both sets of arguments (Figure 2). Moreover, a cell entitled “variable types and dimensions” is included at the beginning of each subroutine; the comments attached to these cells contain the commands relative to declaration and dimensioning of variables.

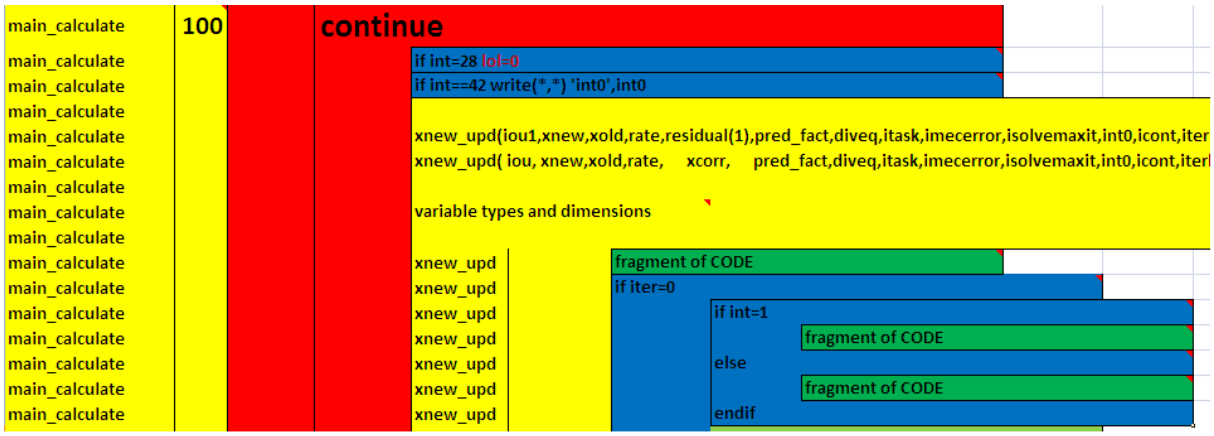

Figure 2: fragment of the flowchart: subroutine xnew_upd is called, which is inside two loops and the subroutine main_calculate

2.2 Color convention

The following convention is used:

1. Yellow is for subroutines.
2. Red is for loops of the form **do-enddo**, **continue-goto**. When the operations made inside the loop are brief enough, the entire text of the loop is transcribed within a single cell.
3. Blue is for logical conditions of the form **if-endif**, **if-elseif-endif**, etc. When the operations made inside the logical condition are brief enough, the entire text of the condition is transcribed within a single cell.
4. Green is for lines of the program. Dark green is for cells whose attached comments contain fragments of the program.
5. Brown is for functions.
6. Different colors are associated to each one of the files that compose the CODE-BRIGHT FORTRAN Project.

2.3 Comments

Many of the cells of the flowchart are commented (Figure 3). The text of the comments can be visualized just by moving the cursor over the area of the corresponding cell. One of the criteria that have been followed during the preparation of the flowchart is as follows: the structure of the flowchart must be such that the size of each comment box does not exceed the dimensions of the screen of a conventional PC. The objective was reducing the amount of mouse operations needed to cover the flowchart.

The comments contain fragments of the program, sets of commands for declaration and dimensioning of variables and remarks that may be useful to the reader.

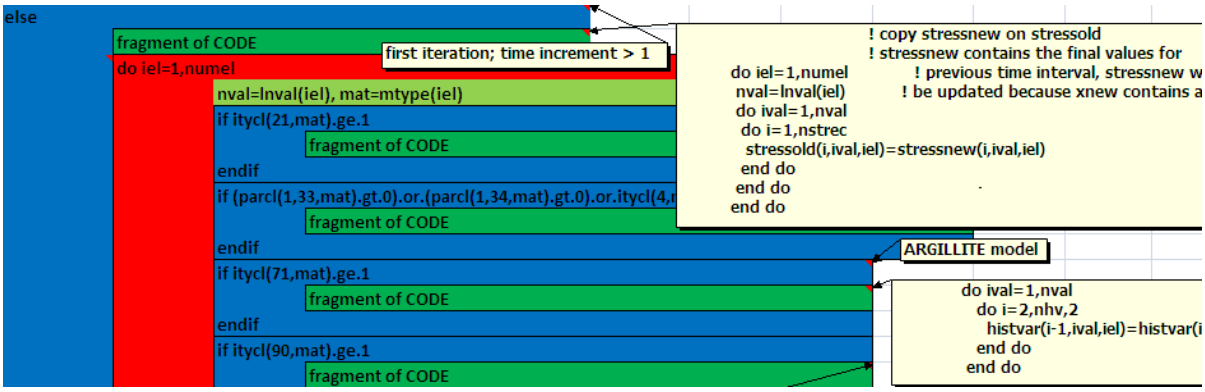

Figure 3: comments attached to the cells of the flowchart may contain fragments of the program, remarks, etc

2.4 Scope of the current version of the Flowchart

For the current version of the flowchart, the values of some variables have been prescribed; as a consequence, certain parts of the program have become disabled and do not appear in the flowchart. The disabled options are not commonly used when working with the version v3beta of CODE-BRIGHT, and have been deleted for the sake of simplicity. More specifically, we have assumed: ISOLVE=3 or 5, IREFIN=0, IUPDPOR=0, IUPDC=0, IOPTHOM=0, IOPTPG=0 or =1, IOPTPC=-1, IOPTXWG=0, IOPTXAL=0, IOPTXHL=0, IOPTXWS=0, IFLAG1=0, IFLAG2=0, IFLAG3=0, IFLAG4=0, IFLAG5=0. The CODE-BRIGHT Manual[iv] contains information about these options.

On the other hand, the contents of the subroutines in the file constitute.f have not been included in the flowchart.

3 CONCLUSIONS AND FUTURE DEVELOPMENTS

We have presented a flowchart of CODE-BRIGHT that may provide users and programmers with a new tool for studying the structure of the program. More information about the flowchart will be soon included in the Manuals of CODE-BRIGHT, and other more schematic versions of it will be available for a progressive learning of the beginners.

On the other hand, the possibility of making some changes in the fundamental architecture of CODE-BRIGHT is to be studied by the authors: restructuration of the assembling subroutines, implementation of new solvers (multi-frontal schemes, for instance), creation of modules for making easier the implementation of new constitutive models, etc.

REFERENCES

[i] Olivella, S., J. Carrera, A. Gens, E. E. Alonso, 1994. Non-isothermal Multiphase Flow of Brine and Gas through Saline media. Transport in Porous Media, 15, 271:293

[ii] Gens, A., 2010, Soil–environment interactions in geotechnical engineering. Géotechnique, 60-1, 3:74.

[iii] CODE-BRIGTH, version v3beta (source code).

[iv] CODE-BRIGHT, Manual, User's Guide, accessible at http://www.etcg.upc.edu/recerca/webs/code_bright/v3/Cb_v3manual_v3.zip/view

CO_2 INJECTION IN DEEP SALINE SLOPING AQUIFERS THROUGH A VERTICAL WELL

Victor Vilarrasa[1,2], Sebastia Olivella[2] and Jesus Carrera[1,3]

[1] GHS, Institute of Environmental Assessment and Water Research (IDAEA), CSIC, Jordi Girona 18-26, 08034 Barcelona, Spain
[2] Dept Geotechnical Engineering and Geosciences, Technical University of Catalonia (UPC-BarcelonaTech), Jordi Girona 1-3, 08034 Barcelona, Spain
[3] Energy City Foundation (CIUDEN), Spanish Government CO_2 Geological Storage Programme, Avenida de Compostilla 2, Ponferrada 24400, Spain

INTRODUCTION

Anthropogenic CO_2 emissions are expected to continue to increase worldwide in the next decades. This could dramatically increase CO_2 concentrations in the atmosphere. One potential mitigation action is CO_2 permanent storage in deep saline aquifers. CO_2 is injected as a supercritical fluid (temperature and pressure higher than 31.1 ºC and 7.38 MPa, respectively) so as to obtain a relatively high density that minimizes the volume occupied by this greenhouse gas. CO_2 density is highly dependent on temperature and pressure because of its high compressibility (Vilarrasa *et al*., 2010a), adopting a wide range of values (450-800 kg/m^3). Since CO_2 is lighter than brine, flow is affected by buoyancy.

Buoyancy produces an upslope migration of the CO_2 bubble in sloping aquifers. The post-injection fate of CO_2 in sloping aquifers has been investigated (e.g. Hesse *et al*., 2008; Elenius *et al*., 2010) but without considering the actual shape of the CO_2 bubble at the end of injection. However, the shape of the CO_2 bubble at the end of injection affects its posterior evolution (McMinn & Juanes, 2009). Gasda *et al*. (2008) studied the effect of a slope up to 1º during the injection period using a 2D model, which represents injection through a horizontal well. However, CO_2 injection through a vertical well, which implies a 3D geometry, has not yet been investigated.

CO_2 will be injected in the Hontomín CO_2 pilot storage site, Burgos (Spain). Hontomín is the site for the CO_2 storage Technology Demonstration Plant (TDP) of the Compostilla OXYCFB300 project, operated by Energy City Foundation (CIUDEN). CO_2 will be injected through a vertical well in a flank of a dome-like structure with a slope close to 20º at a depth around 1450 m. CO_2 injection tests are aimed to gain knowledge on trapping mechanisms and CO_2 bubble and pressure evolution. Pressure evolution is important for assessing the caprock integrity and to avoid the open up of preferential paths for CO_2 leakage (Vilarrasa *et al*., 2010b, 2011). These processes are relatively well known in horizontal aquifers, but a high uncertainty still exists in sloping aquifers.

IMPLEMENTATION OF CO_2 MODULE IN CODE_BRIGHT

CODE_BRIGHT has been adapted to simulate CO_2 injection. To do so, an equation of state for CO_2 has been implemented. CO_2 density follows a Redlich-Kwong equation of state type with the parameters proposed by Spycher *et al*. (2003). CO_2 viscosity has been taken from Altunin & Sakhabetdinov (1972). These expressions for CO_2 density and viscosity are valid regardless of the temperature and pressure conditions (Figure 1).

Additionally, water density increase due to CO_2 dissolution has been implemented following Garcia (2003).

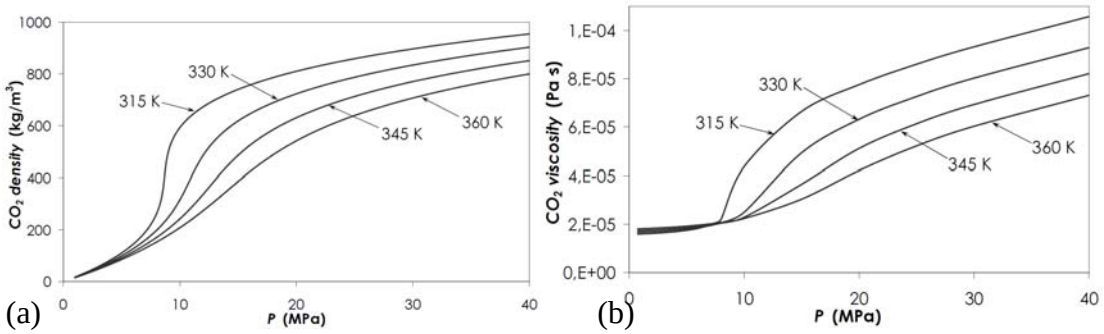

Figure 1. (a) CO_2 density and (b) viscosity as a function of pressure for several temperatures.

MODEL SETUP

To model CO_2 injection in a sloping homogeneous aquifer, we use a 3D model. Since we are interested in simulating CO_2 injection tests of 100 t of CO_2 during 1 week, we model half of the domain, 200x70x10 m^3, by making use of the symmetry in the direction of maximum slope. The upslope and downslope boundaries are treated as constant head boundaries. The aquifer permeability is 10^{-13} m^2 and its porosity 0.1. The slope of the aquifer ranges from 0º to 20º. The mesh is structured, made of hexahedrons of 1 m in side. We use the finite element numerical code CODE_BRIGHT (Olivella *et al*., 1994, 1996) modified for CO_2 injection.

GRAVITY NUMBER

Consider the injection of compressible CO_2 in a deep homogeneous horizontal confined brine aquifer through a vertical well. Mass conservation of these two fluids can be expressed as (Bear, 1972)

$$\frac{\partial(\phi S_\alpha \rho_\alpha)}{\partial t} + \nabla \cdot (\rho_\alpha \mathbf{q}_\alpha) = 0\,, \tag{1}$$

where ϕ is porosity, t is time, S_α is the saturation of the α-phase, ρ_α its density, $\mathbf{q}_\alpha$ its volumetric flux and α is either w brine or c CO_2. Momentum conservation is expressed using Darcy's law

$$\mathbf{q}_\alpha = -\frac{k k_\alpha}{\mu_\alpha}(\nabla p_\alpha + \rho_\alpha g \nabla z)\,, \tag{2}$$

where k is intrinsic permeability, k_α is relative permeability of the α-phase, μ_α its viscosity, p_α its pressure, g is gravity and z the vertical coordinate.

To quantify the relative influence of buoyancy we define a gravity number, *N*, as the ratio of gravity to viscous forces. We use the definition of Vilarrasa *et al*. (2010a) but adopted for sloping aquifers

$$N = \frac{2\pi r_{ch} b k \Delta\rho g \sin\theta \rho_{ch}}{\mu_c Q_m}\,, \tag{3}$$

where b is the aquifer thickness, $\Delta\rho$ is the difference between the fluids density, θ is the slope of the aquifer, Q_m is the mass flow rate and the subindex *ch* denotes a characteristic variable.

NUMERICAL SIMULATIONS

We model the injection of CO_2 in a sloping aquifer through a vertical well. This enables to simulate a realistic evolution of the CO_2 bubble, which starts to advance through the top of the aquifer at the beginning of injection due to buoyancy (Figure 2). The CO_2 bubble advances both laterally and downwards as CO_2 pressure increases. The thickness of the aquifer that gets desaturated depends mainly on the aquifer transmissivity and CO_2 flow rate. Once CO_2 injection stops, the CO_2 bubble is displaced upwards due to buoyancy (Figure 2). This produces the migration of the CO_2 bubble through the top of the aquifer. This might be problematic if solubility and capillary trapping do not completely trap the CO_2 in free phase before it reaches a spillpoint (Gasda *et al.*, 2008; Elenius *et al.*, 2010). The length that the CO_2 will reach depends on the gravity number.

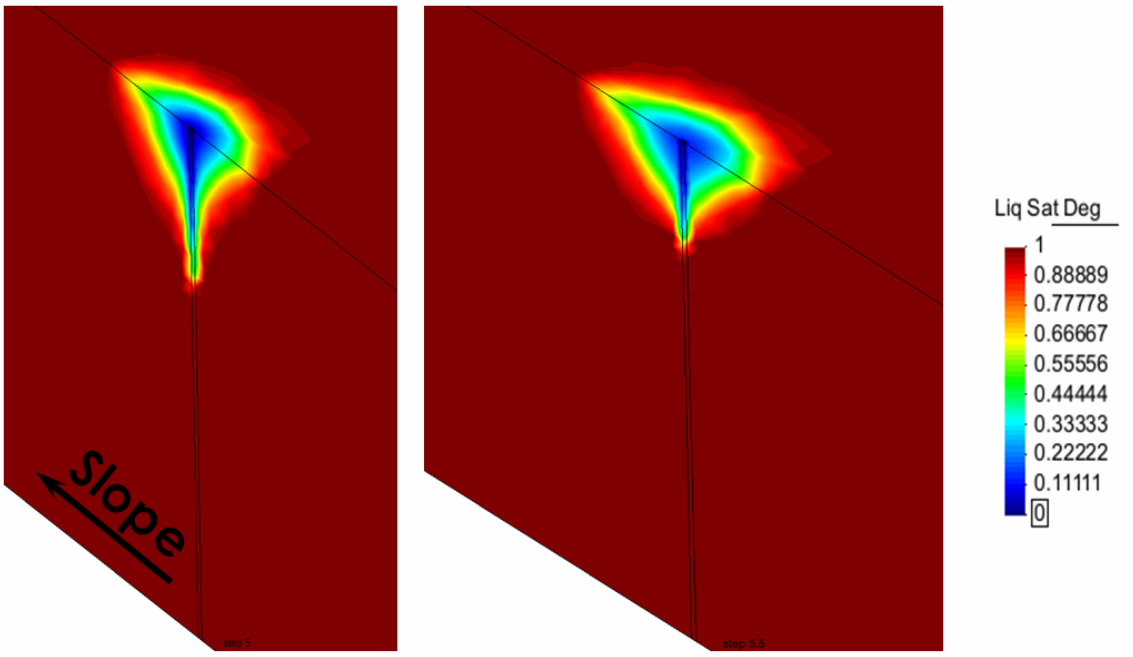

Figure 2. CO_2 bubble after 4 days of a 1 kg/s injection (left) and 0.5 days after injection stops (right). Note that the CO_2 bubble does not occupy the whole thickness of the aquifer (100 m thick). Note also that the CO_2 bubble is displaced upwards and dispersed laterally due to buoyancy once injection stops, advancing preferentially upslope.

CONCLUSIONS

CODE_BRIGHT has been successfully modified to simulate CO_2 injection in deep saline aquifers. The implemented density and viscosity functions are general and cover the whole range of depths and geothermal gradients of potential aquifers. CO_2 injection in sloping aquifers has been simulated using a 3D geometry.

ACKNOWLEDGEMENTS

V.V. wishes to acknowledge the Spanish Ministry of Science and Innovation (MCI), through the "Formación de Profesorado Universitario", and the "Colegio de Ingenieros de Caminos, Canales y Puertos – Catalunya" for their financial support. Additionally, we would like to acknowledge the Spanish Government (Ministry of Industry, Tourism and Trade) through the CUIDEN foundation (project ALM/09/18; www.ciuden.es) and the 'MUSTANG' project (from the European Community's Seventh Framework Programme FP7/2007-2013 under grant agreement nº 227286; www.co2mustang.eu) for their financial support.

REFERENCES

Altunin, VV & Sakhabetdinov, MA (1972). Viscosity of liquid and gaseous carbon dioxide at temperatures 220-1300 K and pressure up to 1200 bar. *Teploenergetika*, 8:85-89.

Bear, J (ed.) (1972). Dynamics of fluids in porous media. Elsevier, New York.

Elenius, MT, Tchelepi, HA & Johannsen, K (2010). CO_2 trapping in sloping aquifers: high resolution numerical simulations. *XVIII International Conference on Computational Methods in Water Resources*, Barcelona.

Garcia, J.E. (2003). Fluid Dynamics of Carbon Dioxide Disposal into Saline Aquifers. PhD thesis, University of California, Berkeley.

Gasda, SE, Celia, MA & Nordbotten, JM (2008). Upslope plume migration and implications for geologic CO_2 sequestration in deep, saline aquifers. *The IES Journal Part A: Civil & Structural Engineering*, 1(1):2–16.

Hesse MA, Tchelepi HA & Orr FM Jr (2008). Gravity currents with residual trapping. *J. Fluid Mechanichs*, 611:35-60.

MacMinn CW & Juanes R (2009). Post-injection spreading and trapping of CO_2 in saline aquifers: impact of the bubble shape at the end of injection. *Compututational Geoscience*, 13:483-491.

Olivella, S, Carrera, J, Gens, A & Alonso EE, (1994). Non-isothermal multiphase flow of brine and gas through saline media. *Transp. Porous Media*, 15:271–93.

Olivella, S, Gens, A, Carrera, J & Alonso EE, (1996). Numerical formulation for a simulator (CODE_BRIGHT) for the coupled analysis of saline media. *Eng. Computations*, 13:87–112.

Spycher, N, Pruess, K & Ennis-king, J (2003). CO_2-H_2O Mixtures in the Geological Sequestration of CO_2. I. Assessment and calculation of mutual solubilities from 12 to 100°C and up to 600 bar. *Geochim. Cosmochim. Acta*, 67:3015-3031.

Vilarrasa, V, Bolster, D, Dentz, M, Olivella, S & Carrera, J, (2010a). Effects of CO_2 Compressibility on CO_2 Storage in Deep Saline Aquifers. *Transp. Porous Media*, 85(2):619-639.

Vilarrasa, V, Bolster, D, Olivella, S & Carrera, J, (2010b). Coupled Hydromechanical Modeling of CO_2 Sequestration in Deep Saline Aquifers. *Int. J. Greenhouse Gas*, 4(6):910-919.

Vilarrasa, V., Olivella, S. & Carrera, J., 2011. Geomechanical stability of the caprock during CO_2 sequestration in deep saline aquifers. *Energy Procedia*, 4: 5306-5313.

A BRIDGE FOUNDATION ANALYSIS

Damians I.P.[*], Olivella S.[*] and Josa A.[*]

[*] Department of Geotechnical Engineering and Geosciences
Technical University of Catalonia (UPC)
Campus Norte UPC, 08034 Barcelona, Spain
E-mail: ivan.puig@upc.edu

Key words: Bridge foundation, Anthropic soil, Plastic analysis.

Abstract. *This document presents the analysis with CODE_BRIGHT finite element program of a geotechnical case. The problem analyzed is related to a mechanical analysis of soil-structure interaction considering different alternatives for the foundation of a bridge in El Prat de Llobregat (Highway A-2). The comparison of displacements shows that an alternative solution using shallow foundations can be considered in addition to the originally proposed, composed by sheet walls.*

1 INTRODUCTION

In order to validate an alternative design for the foundation of a bridge at the Highway A-2 (see general map in Figure 1.a) different solutions have been analyzed geotechnically developing appropriate numerical models with the finite element program Code_Bright[i].

With the geotechnical analysis performed under different assumptions of calculation it is shown that the shallow foundation (concrete box and strip footing; see Figure 2.b), probably less complex and costly than the deeper one (sheet wall; see Figure 2.a), also satisfies the requirements of stability and strength needed while keeping displacements small.

Furthermore, is not unusual to find potholes near the bridge access, generated by the stiffness of the support structure against the settlements of the embankment on the access areas. The contact between the soil and the structure may develop shear stresses which limit the consolidation of the soil near the structure. This may produce an abrupt change on the pavement surface. The found behavior for shallow solution shows that the displacements can be in these zones smoother than in the case of deep foundation, thus reducing the bump effect of the potholes.

The cases have been calculated including plastic behavior (with Cam-Clay model in some materials) and elastic behavior for others. In addition, the presence of groundwater has also been considered in the analysis.

2.1 Model features: materials, properties and tension solicitations

Different laboratory tests carried out on samples taken from soil and characteristic properties have been selected for each material[ii]. The soil types that appear in the test area, according to information drawn from surveys (see geological section on Figure 1.b) can be classified into three types: anthropic fills (a way to describe recent filling materials of different origins), sand with a variable content of fines, and gravel with sand. Anthropogenic

filling has a high dispersion of parameters; this dispersion on the values forces us to assume conservative values. The replacement of the bad quality filling material below the foundation by clean gravel (see Figure 2.b and Table 1 for the parameters) that contributes to a better behavior generating less and uniform settlement has also been considered. Furthermore, another material for the leveling of the surface has been considered, adequately compacted and suitable for the layer required under the pavement. The properties and parameters that have been assumed for the materials that compose the different types of model materials are shown in Table 1.

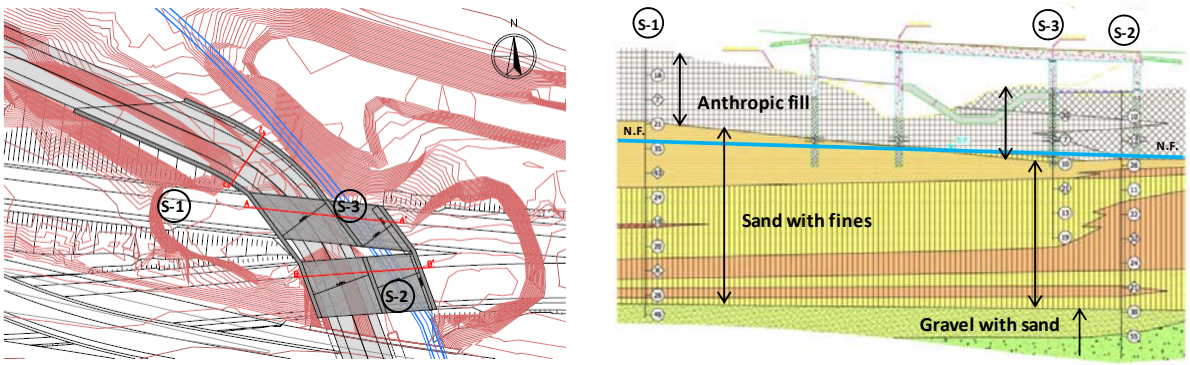

Figure 1: a) General location, **b**) Geologic section of the soil.

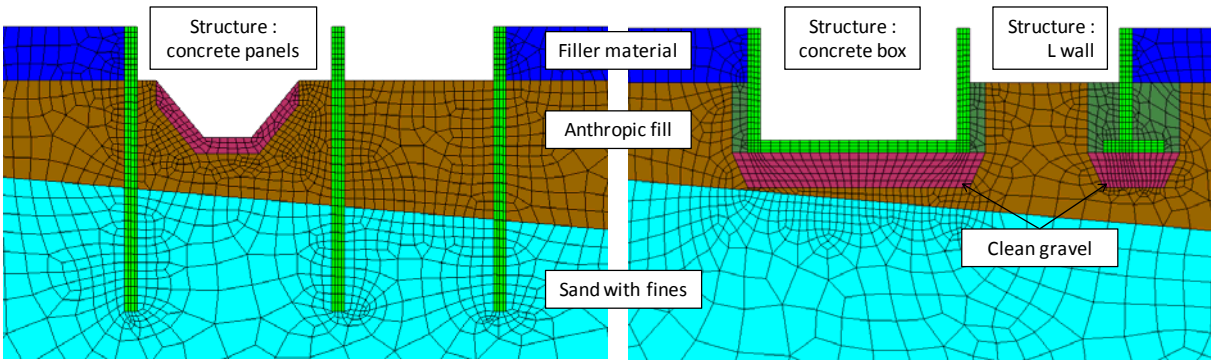

Figure 2: Geometry and finite element mesh of cases to analyze: **a**) Deep foundations with sheet wall, **b**) Shallow foundations with box and strip footing.

Table 1: Constitutive parameters of the materials

Parameters	Materials					
	Anthropic fill	Sand with fines	Gravel with sand	Concrete	Clean gravel	Filler material
E	(5.5 MPa)	-	150 MPa	25000 MPa	15 MPa	50 MPa
□′	26º	28º	-	-	-	-
M	1.03	1.13	-	-	-	-
C_c	0.15	0.12	-	-	-	-
C_s		0.0135 (oc)	-	-	-	-

In Table 1, E is the Young Modulus: it has been obtained from a geotechnical report or suitable for the objective and conservative evaluation; □′ is the effective friction angle: the adopted values are the most conservative values from the different tests and has been considered that cohesion is negligible in all cases; C_c is the compression index; C_s is the swelling index: shows that the material for the sand with variable presence of fines has a bit

of overconsolidation, M is the slope of the critical state line in the plane of invariants (this is, the relationship between isotropic and shear stresses). Poisson ratio value is considered 0.3 for the soil materials and 0.15 for the concrete.

Anthropic fill and sand with variable content of fines soils have been considered with plastic behavior. This means that shear strength (M) and plastic compressibility are required (C_c or λ).

Self-weight of the structure, a distributed load due to normal traffic and point loads due to the presence of a heavy vehicle have been considered in the analyses. The values to be applied on the vertical structures (Figure 2) derived from these three types of loads are shown also in Table 2. The final stage of calculation and the results obtained below correspond to the combination of all these three loading types, i.e. maximum loading conditions.

Table 2: Value of the applied loads

Load Type	Central Support	Central Support	Right Support	Units
Self-weight of bridge: 15 kPa	98	173	75	kN/m
Traffic loads (distributed): 8 kPa	52	92	40	kN/m
Heavy vehicle (point): 600 kN	86	86	86	kN/m

2.2 Results

Figure 3 shows a comparison of displacements obtained from the analyses, considering the self-weight, permanent loads over all surface and the point loads over the three supports. Displacements are somewhat larger for the case of shallow foundation that is in more solidarity with the ground settlements.

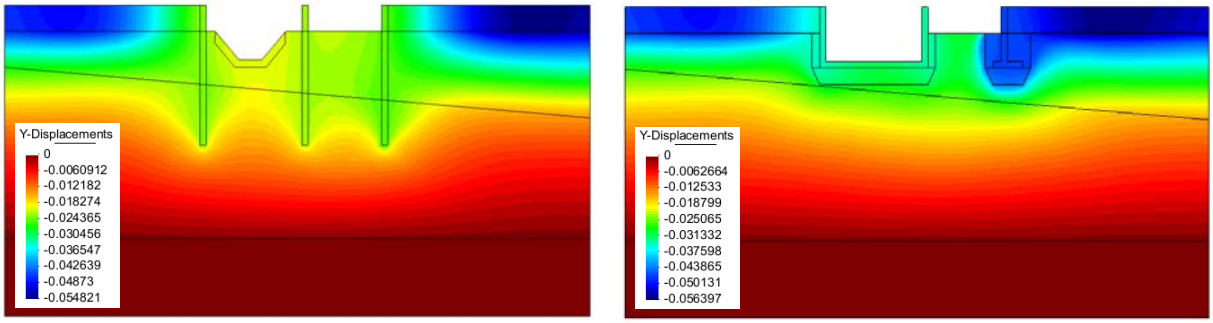

Figure 3: Vertical displacement for the plastic analysis.

In order to illustrate the critical zones in this type of problems, Figure 4 and Figure 5 show the distribution of volumetric and shear plastic deformations generated by the overloading. In the case of sheet walls plastic deformations concentrate around the end of the sheet indicating the zone of support (local failure with a plasticized bulb). In the case of shallow foundation, the gravel fill transmits a stress that produces plasticization of the soil. This plasticization is local and does not show a global failure mechanism.

The results of the vertical displacements calculated with a model that considers the presence of water in the ground according to the geological section shown in Figure 1, are presented in Figure 6. Displacements are similar than in the case of dry soil, but shear deformations show a somewhat different distribution.

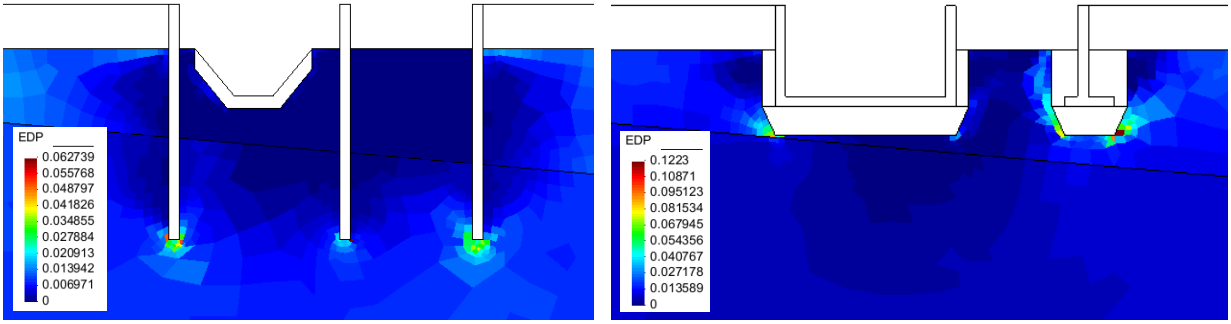

Figure 4: Shear plastic deformation due to the overloading.

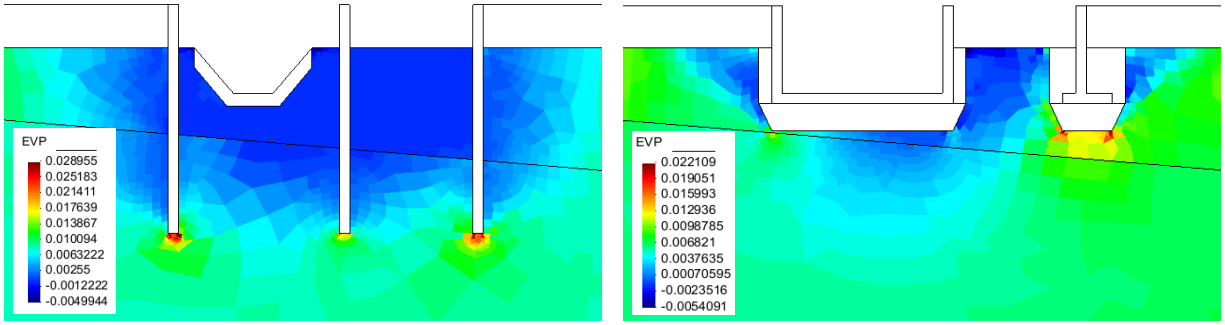

Figure 5: Volumetric Plastic deformation due to the overloading.

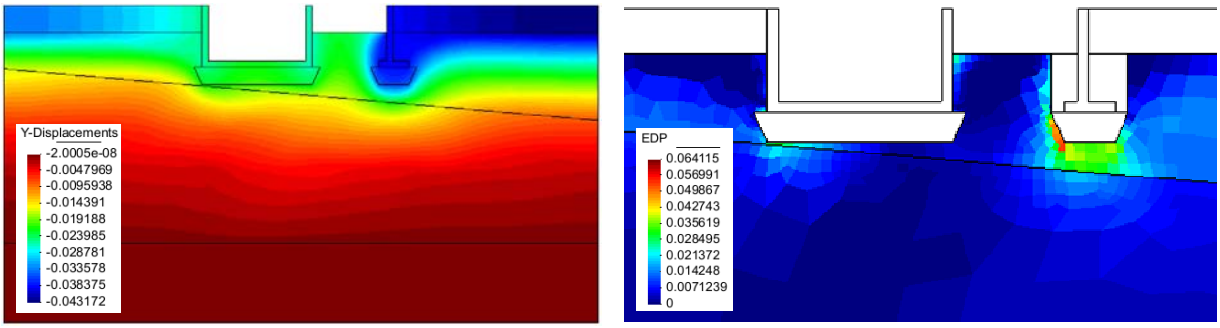

Figure 6: Vertical displacement and plastic strains for the case in which groundwater is considered.

2 CONCLUSIONS

CODE_BRIGHT has proved to be an appropriate tool for calculating the mechanical and comparative analysis of the proposed cases. From the results it seems that the solution by shallow foundations is as valid as the one composed by sheet walls to support the structure and to keep movements in normal range. The final results of the settlements show that the solution by shallow foundation produces movements of the ground surface more uniform than in the case of the sheet walls. This is expected to reduce the effect of potholes that eventually may appear near the entrances of bridges.

3 REFERENCES

[i] Damians I.P., Olivella S., 2010. Informe Técnico: *Cimentación de un paso elevado en la autovía del nordeste (Tramo: El Prat del Llobregat). Análisis de la Interacción Terreno-Estructura*. Universidad Politécnica de Catalunya. Barcelona.

[ii] GEOPAYMA, 2009. Proyecto Modificado: *Mejora del Enlace Autovía A-2, P.K. 0+611.0, tramo: El Prat del Llobregat. Geotecnia*. GEOPAYMA S.A.U. Barcelona.

MODELLING THE EXCAVATION OF THE HG-A MICROTUNNEL

D.Arnedo, S.Olivella and E.E. Alonso

Department of Geotechnical Engineering and Geosciences
Technical University of Catalonia (UPC)
Campus Norte UPC, 08034 Barcelona, Spain
e-mail: diego.arnedo@.upc.edu

Key words: excavation, claystone, anisotropy, bedding

Abstract. *The HG-A in situ experiment is being performed by NAGRA at the Mont Terri underground research laboratory. A micro-tunnel of 1m diameter was excavated in Opalinus Clay. The drilling was performed parallel to the bedding planes. The aim of the test is to monitor the creation and evolution of the excavation damage zone around the micro-tunnel, to asses the variations in the hydromechanical behaviour of Opalinus Clay, with especial focus on its flow properties, and to observe its impact in the gas migration properties during gas injection phase. Here, the simulation of the excavation of the microtunnel is presented.*

1 INTRODUCTION

With the objective of understanding the gas flow processes through argillaceous rocks in schemes of radiaoactive waste disposal, the HG-A in situ experiment [i] was planned and is being performed by NAGRA at the Mont Terri underground research laboratory. Figure 1 shows a layout of the test. A micro-tunnel of 1m diameter was excavated in Opalinus Clay departing from a niche in the 2004 gallery. The drilling was performed parallel to the bedding planes, which have a dipping angle of 45º to SE. The aim of the test is to monitor the creation and evolution of the excavation damage zone around the micro-tunnel, to asses the variations in the hydro-mechanical behaviour of Opalinus Clay, with especial focus on its flow properties, and to observe its impact in the gas migration properties during gas injection phase. The experiment main stages are: tunnel excavation; tunnel backfill and emplacement of instrumentation; packer inflation and backfill saturation; gas injection tests; and a second campaign of hydraulic tests.

2 NUMERICAL MODEL

A 3D hydro-mechanical numerical model of the test using CODE_BRIGHT [ii] is presented. The domain considered for the modelling together with the mechanical and hydraulic boundary conditions (estimated in situ stresses and hydrostatic pore water pressure) are shown in figure 2.

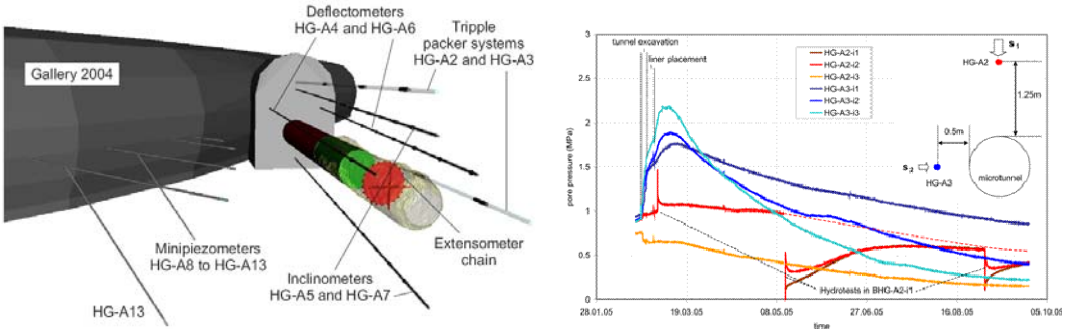

Figure 1. Left: 3D Layout of the HG-A experiment showing the excavated micro-tunnel with the megapacker installed (in green) and the backfilled test interval (transparent). The instrumentation around the tunnel (boreholes) and inside the backfilled section (in red) are included. Right: water pressure evolution at different intervals of boreholes HG-A2 and HG-A3

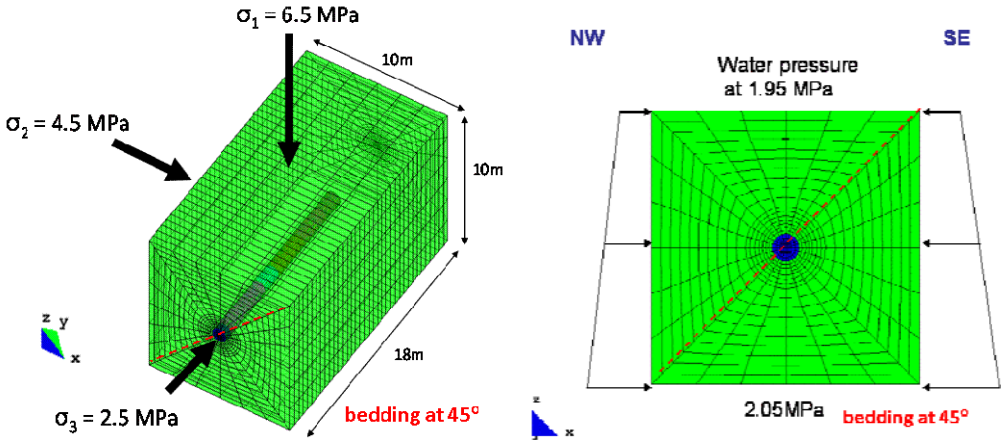

Figure 2. 3D model geometry including mechanical and hydraulic boundary conditions considered in the simulations.

Figure 3 shows the excavation steps considered in the simulation. After the excavation of micro-tunnel, a period of 110 days of drainage is considered by applying an atmospheric water pressure on the microtunnel wall. A linear elastic cross anisotropic constitutive model is considered for the Opalinus Clay. The Young modulus perpendicular to bedding is 4000MPa, while parallel to bedding is 10000MPa. Permeability anisotropy is also taken into account ($5 \cdot 10^{-20}$ m^2 parallel to bedding, one order of magnitude lower in perpendicular direction).

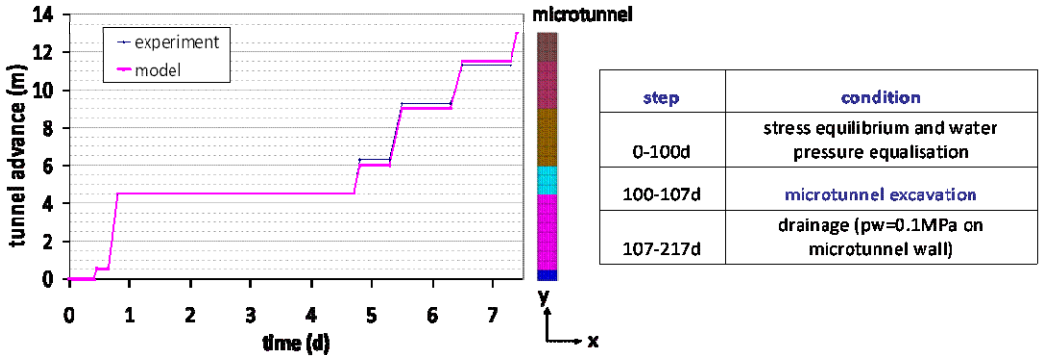

step	condition
0-100d	stress equilibrium and water pressure equalisation
100-107d	microtunnel excavation
107-217d	drainage (pw=0.1MPa on microtunnel wall)

Figure 3. Excavation of microtunnel and analysis steps.

3 SIMULATION RESULTS

Figure 4 shows the evolution of pore water pressure at several nodes located at 1m around the microtunel wall which belong to a vertical section at 7m from the microtunnel entrance. Nodes located parallel to bedding with respect to the tunnel axis (points 4 and 8) develop an increase of water pressure during excavation stage. The opposite is observed at nodes located perpendicular to bedding (points 2 and 6). The mechanical anisotropy leads to higher deformation perpendicular to bedding which explains the different response depending on the orientation with respect to the tunnel axis. During the drainage stage the water pressure response is reversed, due to hydraulic anisotropy. This behaviour is in accordance with the trends observed in the in situ test.

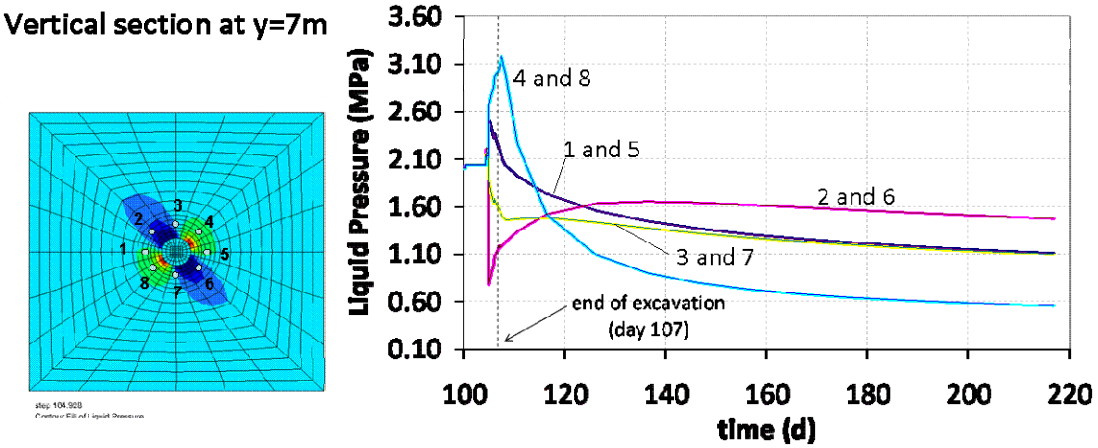

Figure 4. Computed water pressure evolution at points around the microtunnel

Figure 5 shows the porosity fields at the end of excavation and after the drainage stage. Due to the mechanical constitutive model considered, only slight vartiations of porosity are computed. An increase is observed in the zones around the microtunnel orientated perpendicular to bedding with respect to microtunnel axis. A decrease is computed in the zone parallel to bedding with respect to the tunnel axis. Higher variations more representative of an excavation damage zone would be obtained if some features of the Opalinus Clay behaviour, such as plasticity or damage, were considered.

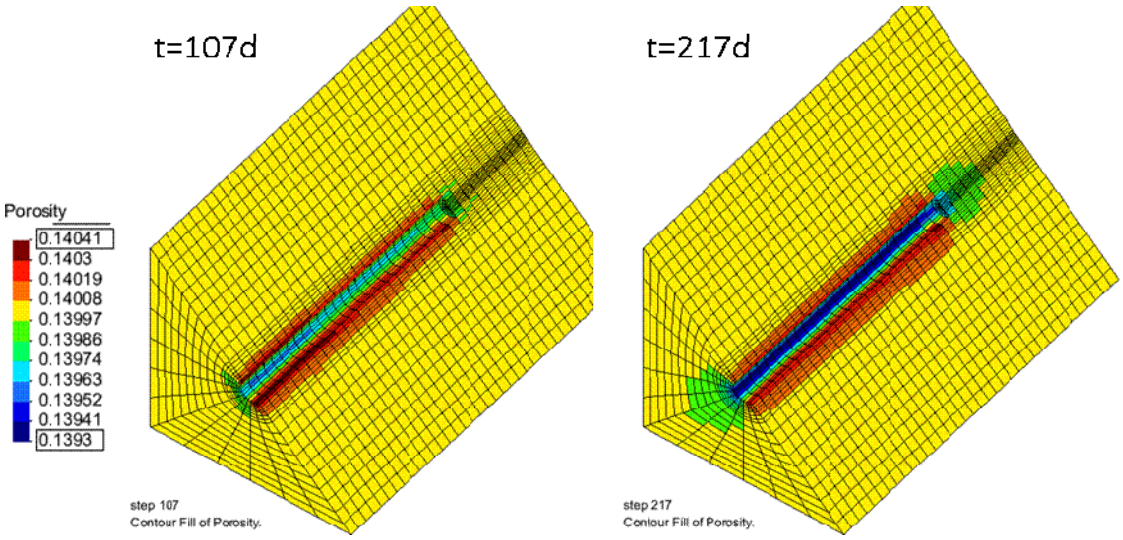

Figure 5. Porosity field at the end of excavation and after the drainage stage. Cut perpendicular to bedding.

4 SUMMARY

A 3D hydro-mechanical model for the excavation of the HGA in situ test microtunnel has been presented. The hydro-mechanical anisotropy of the constitutive model considered explains the observed different responses in pore water evolution depending on the orientation of the observation points with respect to bedding direction and the tunnel axis.

5 REFERENCES

[i] Marschall, P., M. Distinguin, H. Shao, P. Bossart, C. Enachescu & T. Trick. (2006). Creation and Evolution of Damage Zones Around a Microtunnel in a Claystone Formation of the Swiss Jura Mountains. SPE Paper 98537.

[ii] Olivella, S., A. Gens, J. Carrera, E. E. Alonso, 1996, 'Numerical Formulation for a Simulator (CODE_BRIGHT) for the Coupled Analysis of Saline Media', Engineering Computations, Vol 13, No 7, pp: 87-112.

PORE WATER PRESSURE RESPONSE IN RESERVOIR VALLEYS: ANALYSIS OF DRAWDOWN IN CANELLES LANDSLIDES

Núria M. Pinyol[*†] and Eduardo E. Alonso[†]

[*] Centre Internacional de Mètodes Numèrics en Enginyeria
Department of Geotechnical Engineering and Geosciences
Technical University of Catalonia (UPC)
Campus Nord UPC, 08034 Barcelona, Spain
e-mail: nuria.pinyol@.upc.edu

[†] Department of Geotechnical Engineering and Geosciences
Technical University of Catalonia (UPC)

Key words: Drawdown, hydro-mechanical coupling analysis, case history, landslide.

Abstract. *This paper presents an analysis of predicting pore water pressure distribution in slopes located around reservoirs. The problem requires the solution of a coupled flow deformation analysis in a saturated-unsaturated porous media. A fully coupled finite element code, Code_Bright, is used to simulate pore water pressures measured in the left bank of a reservoir (Canelles, Spain) in which a major landslide was triggered in the summer of 2006 by a rapid drawdown.*

1 INTRODUCTION

One of the main problems in the management of reservoir design, construction and operation is the stability of the banks located around the reservoir. Reservoir operation implies two unfavorable effects for the stability of banks and slopes: the inundation of the toe of a potential landslide and the rapid drawdown. Changes in reservoir elevation induce changes in total stress and pore water pressure inside the slope that may affect its stability[i]. Some published real cases of landslides affected by the reservoir water can be mentioned: San Juan de Grijalva Landslide, México 2007[ii]; Qiajiangping Landslide, China, 2003 [iii]; La Josefina Landslide, Ecuador, 1993[iv]; Vaiont Landslide, Italy, 1963[v].

Different simplified approaches have been developed to estimate conveniently the pore water pressure resulting from changes in water level. Field conditions often depart significantly from these simplified approaches. The appropriate analysis becomes a complex problem which requires taking into account the coupled hydro-mechanical effect in a non-saturated media and complex geometries with different kind of materials. These problem are solved by means of advanced numerical tools such as Code_Bright[vi,vii].

The paper presents the analysis of a history case of the left bank of Canelles reservoir (Spain). A large landslide (40×10^6 m^3) was reactivated in the summer of 2006 after a major and rapid drawdown.

2 CANELLES LANDSLIDE

2.1 Introduction and background

During the summer of 2006, after a rapid drawdown a very large landslide developed in the left margin of Canelles reservoir (Catalonia, Spain). Canelles dam, located in the Noguera Ribagorçana river, is 150 m high arch dam.

The geometry of the slide could be established from the detailed analysis of the continuous cores recovered in deep borings and from the limited information provided by inclinometers. Deep piezometric records provided also valuable information on the pressure changes in the vicinity of the failure surface. These data, available for a significant time, allowed validating a flow-deformation coupled calculation model that took into account the changes in water level of the reservoir and external contributions (rainfall). The model indicates that the most likely reason for failure is the rapid drawdown that took place during the summer of 2006.

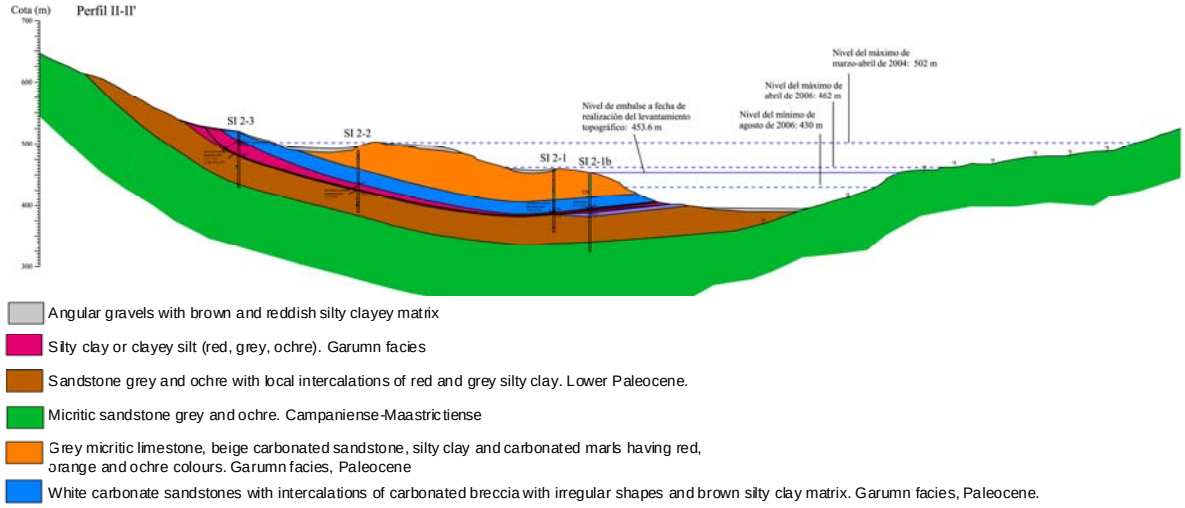

Figure 1. Geological Profile II [v].

2.2 Geological setting and location of the sliding plane

The northern slope of the Sierra de Blancafort consists of sedimentary rocks whose age range from late. Cretaceous to Paleocene. Six groups of materials have been distinguished in the bedrock [viii]. Figure 1 shows a representative geological profile. The identification of the sliding plane was based on several geological indicators.

2.3 Laboratory tests

This section summarizes the results obtained in the laboratory on samples of natural and remoulded material taken from the Garumnian clayey stratum where the failure surface is located. The natural conditions of the samples indicate densities ranging 1.71-1.88 T/m^3. Garumnian clay is quite plastic (w_L = 54-57%; PI = 26-31 %) (CH). Since the landslide is a reactivated slide, the residual strength was measured on remoulded samples in the ring shear equipment. The measured angle ($\phi'_{res} = 12-13^o$) is consistent with the clay plasticity. The permeability to water was also measured in two samples subjected to a vertical stress of 300 kPa. Measured values ranged between 4.2x10^{-10} and 4.9x10^{-11} m/s.

2.4 Water level and piezometer measurements

Figure 2 shows the evolution in time of the water level elevation in the reservoir from January 1987 until 2009. The crack in the left valley slope of the reservoir was observed at the end of summer 2006, after the water level elevation dropped to elevation 430 (absolute minimum value since 1987, according to available data). The average daily drawdown velocity, before failure, was around 0.25 m/day and the daily maximum velocities were higher than 1 m/day during the last drawdown period. Note that the 2006 drawdown followed a long period (1992-2004) in which the level was consistently located above elevation 480. This period probably allowed reaching water pressures corresponding to high water elevations, even in those strata with lower permeability. This previous history should be taken into account when estimating the water pressure during drawdown.

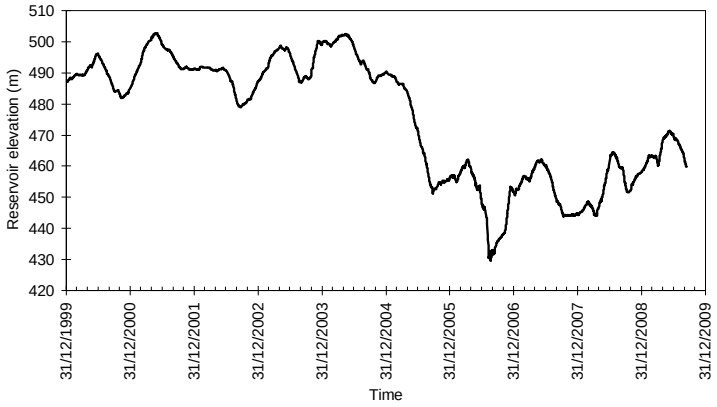

Figure 2. Time evolution of water reservoir elevation.

Five piezometer were installed. Several sensors (three or four) were installed in each bore hole at different depths. Piezometers were located around the clayey layer where the failure surface was most likely to be found

2.5 Pore water pressure calculation

The characterization of the slide, the laboratory tests performed and piezometric measurements seem to indicate that the cause of the sliding was the high water pressures that remained within the low permeability clayey stratum, together with the absence of the stabilising effect of reservoir water due to the drawdown.

The analysis presented here was carried out by means of the finite element code Code_Bright, which can solve coupled flow/deformation problems in saturated/unsaturated media.

The calculation model is shown in Figure 3. The figure also shows a linear quadrilateral element mesh. Nodes have three degrees of freedom (water pressure and vertical and horizontal displacement). The mesh had to be refined mainly in the thinner clay stratum to ensure the correct calculation of water flow through materials in direct contact having values of permeability widely different among them. In order to simplify the model, the sequence of detailed stratification above the Garumnian clay level has not been specified in detail. The mobilised rock above the clay mainly consists of sandstone levels.

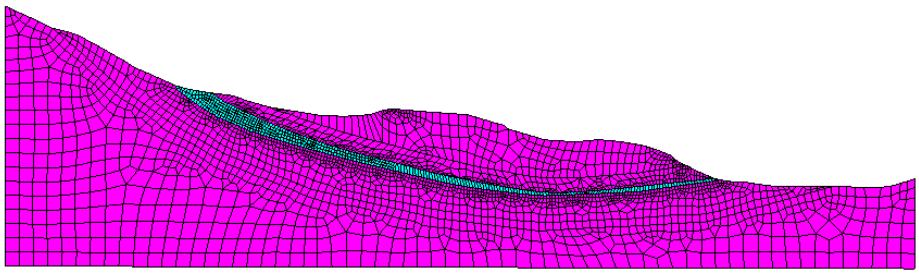

Figure 3. Finite element calculation model.

The stress-strain behaviour of the materials was characterised by means of a linear elastic law. Elasto-plastic considerations have limited effect when estimating drawdown-induced pore water pressure. In addition, the involved materials are highly overconsolidated rocks. Table 1 shows the elastic values chosen, as well as the saturated permeability. Clay parameters were derived from laboratory tests, while rock parameters were estimated according to typical values due of lack of precise data.

Parameter and unit	Clay	Rock
Young modulus (MPa)	500	2500
Poisson's coefficient	0.3	0.3
Saturated permeability (m/s)	$4.9 \cdot 10^{-11}$	10^{-5}
Van Genuchten parameters: P_0	0.3	0.03
λ	0.33	0.33
$S_{r\,max}$	1	1
$S_{r\,min}$	0	0

Table 1. Parameters for coupled hydro-mechanical calculations

The analysis requires the characterization of materials under unsaturated conditions. The retention curves introduced in the calculations use the Van Genuchten model having the parameters indicated in Table 1. Relative permeability is defined according to the cubic law ($k = k_{sat} k_{rel} = k_{sat} S_r^{\,3}$ where k_{sat} is the saturated permeability and *Sr* is the degree of saturation) for both materials.

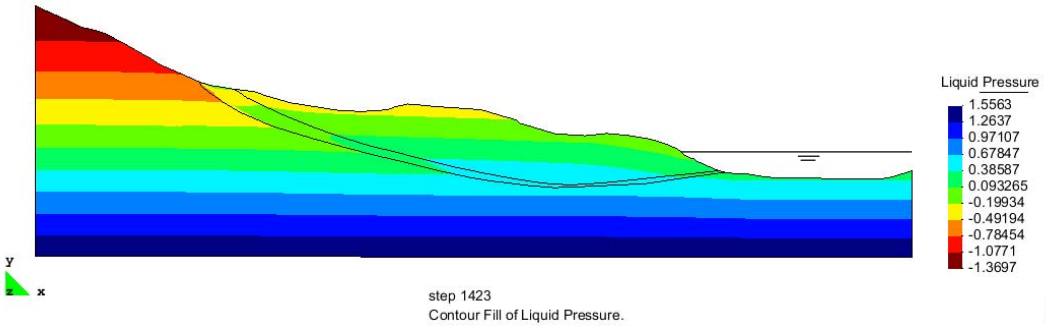

Figure 4. Calculated pore water pressure distribution on August 21, 2006 when reservoir elevation was at 431 m.

The known history of water level elevation, was modelled in the period October, 2002 until July, 2009. This allows establishing the pressures acting on the failure surface with the

purpose of analyzing the stability at any time. In addition, the measurements taken in the piezometers installed in November 2007 could be compared with calculations in an effort to validate the numerical model. The initial pore water pressure assumed in the calculation is a horizontal hydrostatic profile.

The effect of rainfall has been incorporated in the simulation in order to model the water inflow through the upper part of the slope, which is approximately equal to the average value of the rainfall recorded in the region (400 l/m^2/year).

Figure 4 shows the water pressure contours calculated in August 21st, 2006, when water elevation of the reservoir reached elevation 431 m (the minimum values reached in the period 1986 – August 2006). The effect of the low permeability of the clay layer and its continuity can be observed by the abrupt change of the contours.

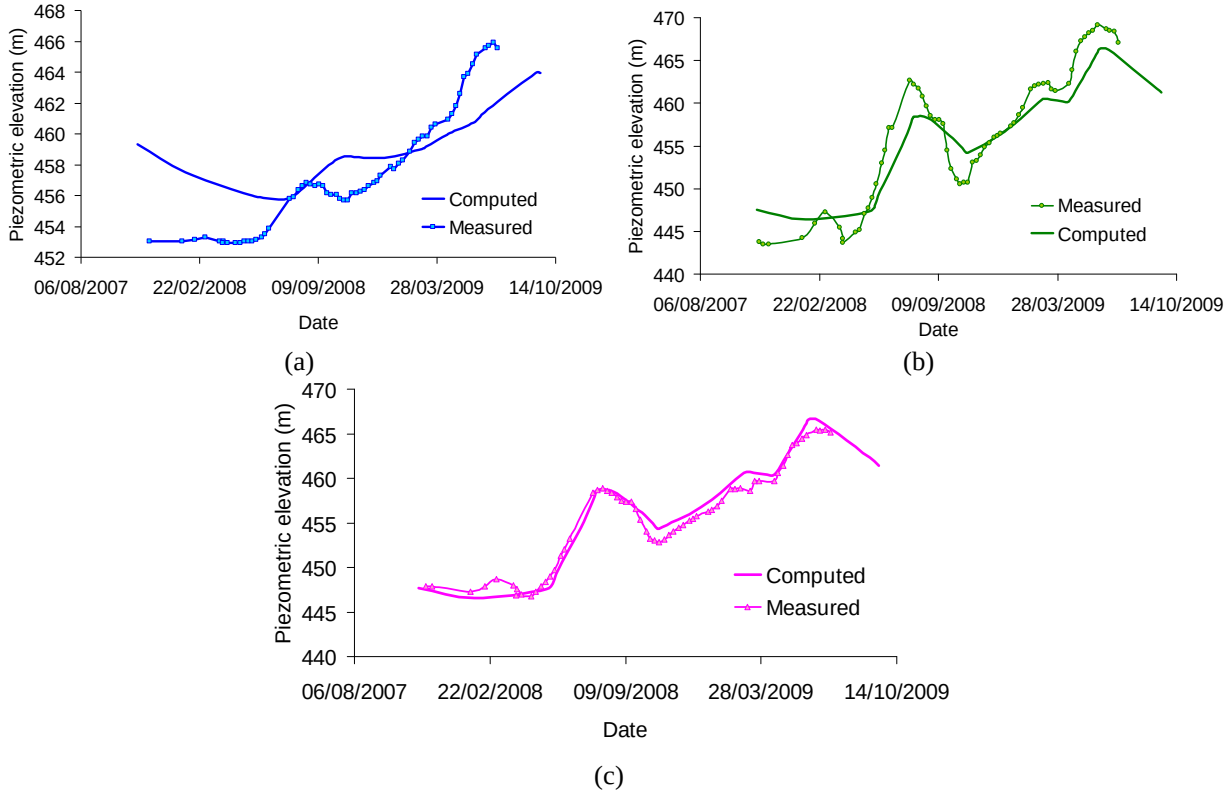

Figure 5. Comparison of calculated and measured pore water pressure in piezometers located in boring SI 2-2 at elevation (a) 429.88 m; (b) 419.88 m; (c) 409.88 m.

The calculated pore water pressure is now compared with piezometer measurement recorded after the failure in order to check the reliability of results. Figure 5 shows such a comparison for the piezometers installed in Profile II. Pore water pressure measured within the lower sandstone in SI2-2, which follow precisely the reservoir elevation evolution, are well captured by the calculation. This is a consequence of a correct choice for sandstone permeability. Pressure measurements within the impervious clayey layer in SI2-2, which are especially important for the subsequent calculation of safety factor, have been simulated quite satisfactorily. Pressures are lightly overestimated when the reservoir reaches low levels.

The major discrepancy appears in piezometers installed in SI2-3. Reservoir level was always below the elevation of piezometers located in SI1-3. In addition, the high sandstone

permeability allows a rapid flow of rainfall infiltration towards the reservoir level. As a result, no positive pore pressures above the piezometer positions are calculated. Field measurements show a totally different response. In fact, water columns in excess of 15–25 m over the piezometers location are measured. This is probably a consequence of the external infiltration and a different local geological structure of pervious/impervious materials at the head of the slide.

3 CONCLUSIONS

Pore water pressures in an initially submerged slope and later subjected to drawdown depend on several soil parameters and external conditions: soil permeability (saturated and unsaturated), soil water retention properties, mechanical soil constitutive behavior, rate of water level lowering and boundary conditions. The paper presents the study of a well documented real case by means of a coupled flow-mechanical analysis valid for saturated and unsaturated conditions using Code_Bright. The comparison between computed results and measurements are quite satisfactory.

REFERENCES

[i] Pinyol, N.M., E.E. Alonso and S. Olivella,, 2008 Rapid drawdown in slopes and embankments. *Water Resources Research* 44, W00D03

[ii] Alcantara-Ayala, I., L. Dominguez-Morales, 2008, The San Juan de Grijalva catastrophic landslide, Chiapas, Mexico: lessons learnt. *Int. Consortium on Landslides*. Casagli, Fanti, Tofani (eds.). Tokyo, Japan, 96-99.

[iii] Wang, F.W., Y.M. Zhang, A.T. Huo, T. Matsumoto and B.T. Huang, 2004, The July 14, 2003 Qianjiangping landslide, Three Gorges Reservoir, China. *Landslides* 1, 157-162.

[iv] Schuster, R.L., D.A. Salceedo and L. Valenzuela, 2002, Overview of catastrophic landslides of South America in the twentieth century. *Catastrophic Landslides: Effects, Occurrenes and Mechnism*. Evans, S.G. and DeGraff, J.V. (eds.) Geological Society of America.

[v] Hendron, A. and F.D. Patton, 1985, The Vaiont slide, a geotechnical analysis based on new geologic observations of the failure surface. *Technical Report* GL-85-5. Department of the Army US Army Corps of Engineers, Washington, DC.

[vi] Corominas, J. and J. Moya, 2010, Informe del deslizamiento de la margen izquierda del embalse de Canelles. *Internal Report*.

[vii] Olivella, S.,A. Gens, J. Carrera, E.E. Alonso, 1996, Numerical Formulation for a Simulator (CODE_BRIGHT) for the Coupled Analysis of Saline Media Engineering. *Computations*, 13 (7), 87-112.

[viii] Olivella, S., J. Carrera, A. Gens, E. E. Alonso, 1994. Non-isothermal Multiphase Flow of Brine and Gas through Saline media. *Transport in Porous Media*, 15, 271:293